

# Migration in the shearing sheet and estimates for young open cluster migration

Alice C. Quillen<sup>1</sup>, Eric Nolting<sup>1</sup>, Ivan Minchev<sup>2</sup>,  
Gayandhi De Silva<sup>3,4</sup> & Cristina Chiappini<sup>2</sup>

<sup>1</sup>*Department of Physics and Astronomy, University of Rochester, Rochester, NY 14627 USA*

<sup>2</sup>*Leibniz-Institut für Astrophysik Potsdam (AIP), An der Sternwarte 16, D-14482, Potsdam, Germany*

<sup>3</sup>*Australian Astronomical Observatory, 105 Delhi Rd, North Ryde, NSW 2113, Australia*

<sup>4</sup>*Sydney Institute for Astronomy, School of Physics, A28, The University of Sydney, Sydney NSW 2006 Australia*

21 March 2022

## ABSTRACT

Using tracer particles embedded in self-gravitating shearing sheet N-body simulations, we investigate the distance in guiding centre radius that stars or star clusters can migrate in a few orbital periods. The standard deviations of guiding centre distributions and maximum migration distances depend on the Toomre or critical wavelength and the contrast in mass surface density caused by spiral structure. Comparison between our simulations and estimated guiding radii for a few young super-solar metallicity open clusters, including NGC 6583, suggests that the contrast in mass surface density in the solar neighbourhood has standard deviation (in the surface density distribution) divided by mean of about 1/4 and larger than measured using COBE data by Drimmel and Spergel. Our estimate is consistent with a standard deviation of  $\sim 0.07$  dex in the metallicities measured from high-quality spectroscopic data for 38 young open clusters ( $< 1$  Gyr) with mean galactocentric radius 7–9 kpc.

**Key words:** Galaxy: disc – Galaxy: kinematics and dynamics – Galaxy: evolution

## 1 INTRODUCTION

In most cases, the stellar surface abundances reflect the composition of the interstellar medium at the time of their birth; so stars can be viewed as fossil records of galaxy evolution. Open clusters abundances probe the chemical evolution of the Galactic thin disc (e.g., Janes 1979; Friel 1995; De Silva et al. 2006; Friel 2010; Pancino et al. 2010; Yong et al. 2012; Magrini et al. 2015; Jacobson et al. 2016; Netopil et al. 2016; Anders et al. 2017; Cantat-Gaudin et al. 2016; Magrini et al. 2017; Casamiquela et al. 2017a,b). From cluster ages, their abundances and galactocentric radii, the galactocentric radial metallicity gradient, the metallicity scatter and the time evolution of these quantities (e.g., Loebman et al. 2016; Jacobson et al. 2016; Netopil et al. 2016; Anders et al. 2017) can be compared to chemical evolution models (e.g., Chiappini et al. 2001; Minchev et al. 2013, 2014) so as to improve understanding of how the Galaxy assembled and evolved.

Nearby and young early B stars in the solar neighborhood are chemically homogeneous, suggesting that the local interstellar medium, from which stars form, is quite homogeneous chemically (Przybilla et al. 2008; Nieva & Przybilla 2012). From the B star homogeneity we infer that mixing

in the interstellar medium is efficient and thorough (e.g., Feng & Krumholz 2014). The nearby B stars have iron abundance  $[\text{Fe}/\text{H}] = 0.02 \pm 0.04$ , equivalent to, within the estimated uncertainties, the iron abundance of the Sun (using values from Table 9 by Nieva & Przybilla 2012 and the Solar iron abundance by Asplund et al. 2009). Slow variations in stellar or gas iron abundance,  $[\text{Fe}/\text{H}]$ , are often described solely with a radial metallicity gradient where the gradient depends on the derivative with respect to galactocentric radius. Migration of stars or clusters from their birth radius (Wielen 1977; Wielen et al. 1996; Sellwood & Binney 2002; Jilkova et al. 2012) broadens local age and metallicity distributions (Roskar et al. 2008; Schönrich & Binney 2009; Stanghellini & Haywood 2010; Loebman et al. 2011; Brunetti et al. 2011; Roskar et al. 2012; Minchev et al. 2013; Haywood 2013; Minchev et al. 2014; Loebman et al. 2016). We use the term *radial migration* to refer to a dynamical process that slowly varies the mean orbital galactocentric radius of a star or cluster that is part of the rotating disc in a disc galaxy. Both stars and star clusters can radially migrate (e.g., Jilkova et al. 2012). The expected chemical enrichment in the last 4 Gyrs is around or below 0.1 dex for

arXiv:1709.04801v3 [astro-ph.GA] 21 Jan 2018

alpha-elements, and around 0.15–0.2 for iron peak elements (Chiappini et al. 2003; Asplund et al. 2009). The presence of super metal rich stars (with  $[\text{Fe}/\text{H}] > 0.25$ ) within the solar neighbourhood (Soubiran 1999) cannot be explained from a baseline chemical evolution model, without requiring radial migration (Chiappini 2009; Casagrande et al. 2011; Minchev et al. 2013).

Open clusters are a setting where observations can be combined to give both age and metallicity measurements. A number of open clusters are so metal rich that they have super-solar metallicities, including NGC 6253 (Carretta et al. 2007; Maderak et al. 2015; Netopil et al. 2016), NGC 6791 (Carretta et al. 2007; Peterson & Green 1998; Casamiquela et al. 2017a), NGC 6583 (Magrini et al. 2010) and NGC 6067 (Alonso-Santiago et al. 2017). Older metal rich open clusters such as NGC 6253 (age 3.3 Gyr, Maderak et al. 2015) or NGC 6791 (age 8 Gyr, Anthony-Twarog et al. 2010) could have been born from initially more metal rich gas located close to the Galactic bulge, and then migrated outward (e.g., Jilkova et al. 2012). Alternatively parent molecular clouds could have been locally enriched by nearby supernovae prior to cluster formation (see discussions by Maderak et al. 2015; Magrini et al. 2015). The two scenarios might be told apart from patterns in  $\alpha$  process and iron peak element abundances. The recent study by Magrini et al. (2017) finds agreement between age, radius and abundance distributions of open clusters and the predictions of chemical evolution models that are based on N-body numerical simulations of a Milky Way-like galaxy that exhibit radial migration (Minchev et al. 2013, 2014).

Young super-solar metallicity open clusters cannot be too far from their birth galactocentric radii as the process of radial migration has less time to operate. Using the values recently tabulated by Bland-Hawthorn & Gerhard (2016), the rotation period at the galactocentric radius of the Sun ( $R_{\odot} \approx 8.2$  kpc) is approximately 210 Myr (using angular rotation rate  $\Omega_0 = 30 \text{ km s}^{-1} \text{ kpc}^{-1}$ ). An open cluster that is 1 Gyr old, such as NGC 6583 (Carraro et al. 2005), would rotate about the Galaxy only approximately 5 rotation periods during its lifetime (using the rotation period near the Sun). The Hyades and Praesepe (NGC 2632) clusters with age approximately 700 Myr (Cummings et al. 2017) have iron abundance  $[\text{Fe}/\text{H}] \approx 0.15$  (Cummings et al. 2017) and ages corresponding to three rotation periods. If these clusters were born at smaller galactocentric radii, the difference between their estimated birth radius and current mean orbital radius must constrain the extent of radial migration possible in a few rotation periods (e.g., see discussion by Bland-Hawthorn et al. 2010).

We focus here on whether and how star or star-cluster radial migration could occur in a Gyr. If a transient spiral pattern grows and decays on a timescale comparable to one half the oscillation period within a horseshoe orbit of the corotation region of a spiral wave, a star or star cluster can be moved from one side to the other side of the corotation resonance. The star or star cluster is left on the other side of resonance if the spiral pattern vanishes before pulling it back (Sellwood & Binney 2002). This mechanism is often called *radial migration* and when caused by stochastic growth and disappearance of transient spiral waves it is sometimes called ‘churning’ (Sellwood & Binney 2002; Roskar et al. 2008; Schönrich & Binney 2009). Additional mechanisms may in-

duce radial migration, such as resonant coupling with bar and spiral arms (Minchev & Famaey 2010; Brunetti et al. 2011) and interference between spiral patterns (Quillen et al. 2011; Comparetta & Quillen 2012).

The radial maximal migration rate is expected to depend on the surface density and amplitude of spiral structure (Sellwood & Binney 2002; Schönrich & Binney 2009; Daniel & Wyse 2015). The 3D stellar structure of the Milky Way based on COBE/DIRBE data (Drimmel & Spergel 2001) found an on-off surface density contrast in the stellar component of the strongest spiral arm (namely the Crux-Scutum arm at a galactic longitude of about  $310^\circ$ )  $(\Sigma_{max} - \Sigma_{min})/\Sigma_{min} \sim 0.32$  and this is below that expected for spiral galaxies similar to the Milky way (of order 1, e.g., Ma 2002). The Glimpse survey observations confirmed the COBE/DIRBE spiral tangent arm detections (Benjamin et al. 2005) but have not yet updated an estimate for the stellar spiral arm surface density contrast. We can consider the amplitude in surface density of spiral structure between  $R_{\odot}$  and the bar end at about 4 kpc as poorly constrained. We ask here: Is the roughly measured amplitude in spiral structure in the Galaxy large enough to achieve migration rates necessary to account for young super-solar metallicity open clusters? The answer to this question would help us differentiate between local enrichment and migration processes, and connect the age, metallicity and orbit distributions of open clusters to migration models.

A number of studies have measured radial migration rates from numerical simulations (e.g., Minchev et al. 2011; Brunetti et al. 2011; Loebman et al. 2011; Roskar et al. 2012; Comparetta & Quillen 2012; Grand et al. 2012; Minchev et al. 2012, 2013, 2014; Loebman et al. 2016; Martinez-Medina et al. 2017). A difficulty of using N-body simulations of an entire galaxy is that underlying parameters such as spiral amplitude are difficult to adjust. Instead of an N-body simulation that simulates an entire disc, we focus on a small patch of the disc using the shearing sheet approximation (Julian & Toomre 1966; Toomre & Kalnajs 1991; Rein & Tremaine 2012); (see Figure 1 and our appendix). The shearing sheet is a model dynamical system that can be used to study the dynamics of astrophysical discs. A self-gravitating shearing sheet exhibits spiral instability (Julian & Toomre 1966; Toomre 1981; Toomre & Kalnajs 1991). The advantage of focusing on a small patch is that the simulation is independent of galactic radius and depends on only a few parameters. We aim to adjust the amplitude of spiral structure to probe how far stars or star clusters can migrate in few rotation periods.

In section 2 we describe our N-body shearing simulations. With these simulations in section 3 we measure changes in the distributions of guiding centre positions and how they depend upon time and the strength of spiral structure in the simulated shearing patch. In section 4 we identify a few metal rich young open clusters. A simple model derived from our simulations is then applied to interpret these open clusters in terms of constraints on the spiral structure that may have mediated their radial migration.

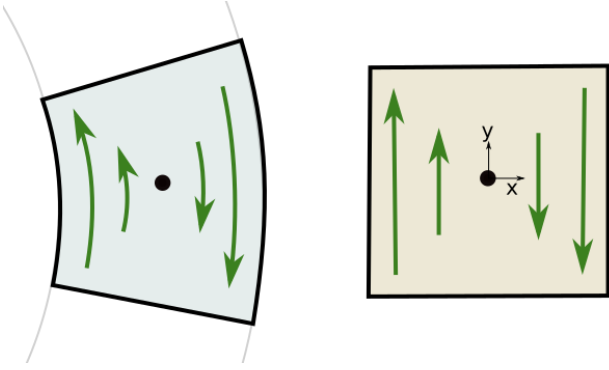


**Figure 1.** An illustration of a patch of a rotating disc (on left) and how the shearing box (on right) approximates it. Arrows are shown with respect to motion in the centre of the disc patch (on left). In this rotating frame a circular orbit would remain fixed at the black dot. An orbit with zero epicyclic amplitude and located at the centre of the shearing box (on right) would also remain fixed. The orientation of our coordinate system is shown on the right.

## 2 SHEARING SHEET N-BODY SIMULATIONS

In this section we describe our shearing sheet simulations, dimensions used to characterise them (section 2.1), how they are set up (section 2.2) and how initial particle positions and velocities are generated (section 2.3).

The shearing sheet (Toomre & Kalnajs 1991) approximates a local patch of a rotating disc (see Figure 1). Our N-body simulations of a disc patch use the N-body code `rebound` (Rein & Liu 2012) that contains an integrator and shear boundary conditions specifically written to simulate a self-gravitating disc patch using the shearing sheet approximation (Rein & Tremaine 2012). From `rebound` we use the Symplectic Epicycle Integrator (SEI) integrator (Rein & Tremaine 2012) and the associated shear boundary conditions. The shear boundary conditions are periodic in two directions,  $x, y$  but open in the third direction  $z$ . This differs from the simulations by Toomre & Kalnajs (1991) that were restricted to two dimensions. A square  $x, y$  area is simulated that we call the shearing box (see Figure 1). Velocity shear (corresponding to differential rotation) is a function of  $x$ , so variations in  $x$  correspond to variations in galactic radius. Variations in  $y$  correspond to variations in azimuthal angle  $\theta$  in the midplane. Galactic rotation corresponds to particles moving in the  $y$  direction. The  $z$  direction is perpendicular to the disc and shearing box. Velocity shear itself depend on the parameters  $\Omega$  and  $\kappa$  which are independent of position within the shearing box. Our notation for these two frequencies follows Binney & Tremaine (1987); Rein & Tremaine (2012) and  $\Omega$  represents the angular rotation rate in the disc, and  $\kappa$  the epicyclic frequency. The parameters  $\Omega$  and  $\kappa$  are independent of position in the shearing box but shear is present in the box and the shearing sheet itself approximates a disc that exhibits radial gradients in both of these frequencies. The gradient of velocity (the velocity shear corresponding to differential rotation) depends on both parameters, as given in equation A3.

Long-range gravitational forces from each particle are computed using the oct-tree approximation based on the al-

gorithm by Barnes & Hut (1986). Ghost-boxes are used to include forces from particles that are nearby taking into account the shearing periodic boundary condition (see section 4.2 by Rein & Liu 2012). Particle collisions are ignored.

The equations of motion in  $x, y$  for the shearing sheet are given in the appendix (see equations A2). Orbits in the plane are described by a guiding centre  $x_g, y_g$ , epicyclic amplitude  $C$  and epicyclic angle  $\phi$ . Variations in  $x_g$  correspond to variations in guiding radius or angular momentum in a full disc. An induced variation in  $x_g$  can be called radial migration. Heating or increasing the in-plane components of the velocity dispersion corresponds to increasing the epicyclic amplitudes (e.g., Jenkins & Binney 1990). Transient spiral structure is expected to cause both heating and migration. However, an individual star that migrates a large distance may not be excited to large epicyclic amplitude and the opposite is also true.

The SEI integrator was written specifically for application in celestial mechanics and so has angular rotation rate equal to the epicyclic frequency;  $\Omega = \kappa$ . We have modified the `rebound` routines `boundaries_shear.c` and `integrator_sei.c` so that the epicyclic frequency can take values  $\kappa \neq \Omega$  allowing us to simulate the shearing sheet corresponding to differential rotation in a galactic disc. Our code modifications from those described by Rein & Tremaine (2012) are described in section A1.

The equations of motion in  $z$  are set by an additional parameter, the vertical epicyclic frequency  $\Omega_z$  (see section A2, section 3.3 by Rein & Liu 2012 and equation 13 and discussion near this equation by Rein & Tremaine 2012). However, the actual vertical epicyclic frequency is somewhat faster than  $\Omega_z$  due to the self-gravity of the disc. The value we list in Table 1 for  $\Omega_z$  is the parameter set in the code.

### 2.1 Dimensions

The natural unit of time for the shearing sheet is  $\Omega^{-1}$ , or the associated orbital period  $P \equiv 2\pi/\Omega$ . With a self-gravitating disc of mean mass surface density  $\Sigma$ , a natural unit of distance is the Toomre wavelength, often called the critical wavelength,

$$\begin{aligned} \lambda_{crit} &\equiv \frac{4\pi^2 G \Sigma}{\kappa^2} \\ &= 1 \text{ kpc} \left( \frac{\Sigma}{10 M_{\odot} \text{ pc}^{-2}} \right) \left( \frac{2}{\kappa^2 / \Omega^2} \right) \left( \frac{\Omega}{30 \text{ km s}^{-1} \text{ kpc}^{-1}} \right)^{-2}, \end{aligned} \quad (1)$$

where  $G$  is the gravitational constant. This wavelength is independent of the particle velocity dispersion. Where there are variations in the surface density  $\Sigma$  we use the mean of the surface mass density distribution,  $\mu_{\Sigma}$ , to compute  $\lambda_{crit}$ . For comparison, the estimated total stellar (including brown dwarfs, white dwarfs and other remnants) surface density in the solar neighbourhood is  $\Sigma_* \approx 33 M_{\odot} \text{ pc}^{-2}$  and in gas  $\Sigma_g \approx 14 M_{\odot} \text{ pc}^{-2}$  with  $\approx 7 M_{\odot} \text{ pc}^{-2}$  in cold molecular and atomic hydrogen near the midplane (McKee et al. 2015). The Galactic disc baryonic components total just under  $50 M_{\odot} \text{ pc}^{-2}$ , similar to previous estimates for the local disc surface density (Flynn et al. 2006).

Shear amplification is strongest at about the Toomre wavelength so a self-gravitating disc most quickly grows spiral structure of this wavelength (Toomre 1981; Athanassoula

1984; Toomre & Kalnajs 1991; Fuchs 2001). We set the box size of the shearing sheet simulation to exceed the Toomre wavelength (as did Toomre & Kalnajs 1991) so that the simulations can resolve this wavelength.

The Toomre  $Q$ -parameter (Safronov 1960; Toomre 1964) for a stellar disc depends on the stellar velocity dispersion with  $\sigma_{vR}$  the standard deviation of its radial component,

$$Q \equiv \frac{\sigma_{vR}\kappa}{3.36G\Sigma} = 1.1 \left( \frac{\sigma_{vR}}{20 \text{ km s}^{-1}} \right) \left( \frac{\kappa/\Omega}{\sqrt{2}} \right) \times \left( \frac{\Omega}{30 \text{ km s}^{-1} \text{ kpc}^{-1}} \right) \left( \frac{\Sigma}{50 M_{\odot} \text{ pc}^{-2}} \right)^{-1}. \quad (2)$$

The amplitude or strength of spiral structure is primarily set by the Toomre  $Q$ -parameter (Fujii et al. 2011). For the shearing sheet simulations we use only the massive particles to compute the standard deviation of the  $x$  velocity component  $\sigma_{vx}$ , and replace  $\sigma_{vR}$  with  $\sigma_{vx}$  to compute the Toomre  $Q$ -parameter.

## 2.2 Simulation set up and drag force

We use massive particles to generate self-gravitating spiral structure. A thousand massless particles embedded within the simulation are used as tracers to track variations in guiding centre position  $x_g$ . Spiral structure induced drifts in tracer particle  $x_g$  values are interpreted as radial migration. Tracer particles are point masses and so can represent stars or compact star clusters. In section 4 we use the results of our shearing sheet simulations to discuss migration of open clusters, assuming that they do not strongly perturb the background Galactic spiral structure and neglecting processes of cluster evaporation and dissolution. We assume that the size of the shearing box significantly exceeds the size of a star cluster.

A disc initially set with Toomre  $Q \gg 2$  will not show spiral structure, whereas one initially set with  $Q \lesssim 1$  will be unstable, allowing spiral structure to grow. As a simulation runs, the spiral structure itself heats the disc and increases the Toomre  $Q$ -parameter. Growth and decay of transient spiral structure induces variations in the epicyclic amplitude of stars (Carlberg & Sellwood 1985; Jenkins & Binney 1990) and this can happen over a range of radius as stars need not be near a Lindblad resonance. The heating rate is faster at low Toomre  $Q$ -parameter values (Fujii et al. 2011). To allow us to run simulations that show high amplitude spiral structure but only slowly vary in Toomre  $Q$ -parameter, we added a small fictitious drag force to the massive particles as an additional force to **rebound** so as to cool the disc. Our drag force is identical to that used by Toomre & Kalnajs (1991) (see the top of their page 350), is a straightforward velocity dependent acceleration in the  $x$  direction

$$a_x = -\alpha\Omega v_x, \quad (3)$$

and is described by a single unitless parameter  $\alpha$  which sets the timescale for damping the epicyclic amplitude. We applied the drag force to massive particles only and only in the  $x$  direction so we did not need to take into account the velocity shear to compute a damping force and so that vertical motions are unaffected. At larger values of Toomre  $Q$ -

parameter and with weaker spiral structure, the heating rate is reduced and so damping was not necessary to maintain a slowly varying Toomre  $Q$ -parameter. Our damping serves as a source of dissipation, replacing hydrodynamic dissipation that would be modeled in more realistic simulations that include a gaseous as well as a stellar disc component. Toomre & Kalnajs (1991) verified that a steady state in the velocity distribution could be reached after many orbits of integration.<sup>1</sup> Our goal is to look at the extent of migration over only a few orbital periods so it is not necessary to maintain exact stability in the character of spiral structure over many orbital periods. However the heating and migration rate are affected by slow variations in the spiral structure and these are present in the simulations. We will discuss this sensitivity later when we study variations in the distributions.

We first choose a number of massive particles to simulate and a mean disc surface density,  $\Sigma$ . The shearing box size is chosen to exceed the Toomre wavelength. The massive particle masses are identical and set using the box size and mean disc surface density.

Common parameters for our simulations are listed in Table 1 and those for individual simulations in Table 2. The rotation curve near the solar neighborhood is nearly flat (see section 6.4 and Figure 16 by Bland-Hawthorn & Gerhard 2016) corresponding to  $\kappa/\Omega \approx \sqrt{2}$ . The value chosen for this ratio (and listed in Table 1) is approximately consistent with the differential rotation of a flat rotation curve.

While it is natural to work with time in orbital periods  $P = 2\pi/\Omega$  and length in units of the Toomre wavelength, it is helpful for interpretation to relate these to actual physical units. The angular rotation rate near the Sun is about  $\Omega \sim 30 \text{ km s}^{-1} \text{ kpc}^{-1}$  corresponding to an orbital period of about 200 Myr (using values by Bland-Hawthorn & Gerhard 2016). Through-out this manuscript we give lengths in units of Toomre wavelength and in pc for a Toomre wavelength of  $\lambda_{crit,0} = 1007 \text{ pc}$  computed for a mass surface density of  $\Sigma_0 = 10 M_{\odot} \text{ pc}^{-2}$ . Equation 1 can be used to estimate distances for another value of mean surface density by multiplying the Toomre wavelength by the desired  $\Sigma$  divided by the value  $\Sigma_0 = 10 M_{\odot} \text{ pc}^{-2}$ . When working in pc, Myr and solar masses, velocities are in  $\text{pc/Myr} \sim \text{km/s}$  and the gravitational constant  $G = 0.0045 M_{\odot}^{-1} \text{ pc}^3 \text{ Myr}^{-2}$ .

## 2.3 Initial conditions for particles

For the massive particles, initial guiding centre coordinates  $x_g, y_g$  are chosen randomly using uniform probability distributions covering the area of the shearing box. The in-plane and vertical epicyclic angles are randomly chosen from uniform probability distributions in  $[0, 2\pi]$ . The in-plane and vertical epicyclic amplitudes are randomly chosen from uniform probability distributions ranging from zero to maximum values. Initial particle positions and velocities are computed from the epicyclic amplitudes and angles and guiding centre coordinates using equations A2 and A11. The resulting massive particle distribution is uniformly distributed in  $x, y$  in the shearing box. So there is no gradient in the mean

<sup>1</sup> At large values of  $\alpha$  and with small softening lengths, clumps can form in the disk (Agris Kalnajs, private communication).

mass surface density  $\Sigma$  in the shearing sheet. The maximum value for the vertical epicyclic amplitude sets the disc thickness, whereas the maximum in-plane epicyclic amplitude sets the initial Toomre  $Q$ -parameter. The number of massive particles and smoothing or gravitational softening length were chosen to be large enough that the simulations are not highly sensitive to either value. We will illustrate how variations in these quantities affect our results in section 3.4. The 2 dimensional shearing sheet simulations by Toomre & Kalnajs (1991) used a larger smoothing length than ours ( $\sim 0.2\lambda_{crit}$ ) perhaps in part to mimic the behavior of disk thickness.

Massless tracer particles are used to measure variations in guiding radius  $x_g$  corresponding to migration. After two rotation periods, the growth rate of spiral structure in the massive particles is reduced. The tracer particles are only added to the simulation after two orbital periods, after which time the amplitude of spiral structure varies less quickly. Tracer particles are added after spiral structure is grown so as to mimic the birth of stars and clusters into a galaxy in which spiral structure is present. After the 1000 tracer particles are added, the simulation is integrated for 5 additional orbital periods. Our figures show time in units of orbital periods from the time when the tracer particles are added to the simulation.

Tracer particles are begun in the plane  $z = 0$  and at  $x = 0$  but with  $y$  values chosen from a uniform distribution covering the width of the shearing box. The initial distribution can be seen in the leftmost panel in Figure 2. The velocity is set to zero so the particle initially has guiding radius  $x_g = 0$ , epicyclic amplitude  $C = 0$  and zero vertical epicyclic amplitude. In the absence of spiral perturbations the tracer particles would remain fixed (see equations A2 and A3). As the tracer particles are massless, their initial linear distribution does not disturb the development and evolution of spiral structure. Because tracer particles are begun with  $x_g = 0$ , the absolute value of the guiding position  $|x_g(t)|$  is an estimate for the distance migrated. As our tracer particles are point masses, the sizes of the clusters that they represent are neglected. The migration distances we consider are similar to or greater than hundreds of pc and so we neglect the much smaller initial cluster size (about 1 pc).

**Table 1.** Common simulation parameters

Number of massive particles	50000
Number of massless tracer particles	1000
Time when tracers are added to simulation	2 orbital periods
Integration time after tracers are added	5 orbital periods
Time step	0.002 orbital periods
$\kappa/\Omega$	1.4
$\Omega_z/\Omega$	1.8
Smoothing length	$0.0496 \lambda_{crit} = 50$ pc
Shearing box length	$3.97\lambda_{crit} = 4.0$ kpc
Massive particle mass	$3200M_\odot$
$\sigma_z$	$0.15\lambda_{crit} = 150$ pc

Notes. In the above Table, dimensions in pc and  $M_\odot$  are given for a disc with  $\Sigma_0 = 10 M_\odot \text{pc}^{-2}$  and Toomre wavelength  $\lambda_{crit,0} = 1007$  pc. Here  $\sigma_z$  is the standard deviation of  $z$  for the massive particles. The circular velocity around one particle at a smoothing length is 0.5 km/s, computed with  $G = 0.0045 M_\odot^{-1} \text{pc}^3 \text{Myr}^{-2}$ .

**Table 2.** List of simulations

Simulation	$Q$	$\alpha$	$\sigma_\Sigma/\mu_\Sigma$	differences
X1	2.4	0.005	0.20	
X2	2.0	0.005	0.22	
X3	1.6	0.005	0.26	
X4	1.4	0.02	0.34	
X5	1.2	0.05	0.46	
X3S	1.6	0.005	0.26	smaller smoothing length
X3N	1.6	0.005	0.32	fewer particles
X3ha	1.6	0.005	0.24	thicker disc
X3hb	1.7	0.005	0.30	thinner disc

Notes. The X3S, X3N, X3ha, X3hb simulations are similar to the X3 simulation except as described in the rightmost column. X3S has half X3's smoothing length, X3N has half X3's number of particles, X3ha has twice X3's disc thickness and X3hb has half X3's thickness. The Toomre  $Q$ -parameter is measured at 2.5 orbital periods after tracer particles are added to the simulation. The ratio of the standard deviation to mean of the surface density distribution  $\sigma_\Sigma/\mu_\Sigma$  is computed at the same time and is a measure of surface density contrast. The drag force for massive particles is set by  $\alpha$ .

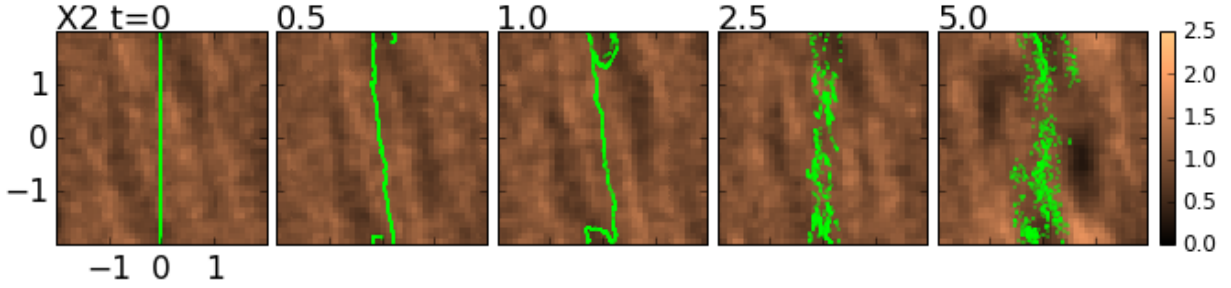


**Figure 2.** Surface mass density of massive particles shown as an image with the positions of 1000 massless tracer particles, shown as green dots, at 5 different times in the X2 simulation. The times for each snapshot are 0, 0.5, 1.0, 2.5 and 5.0 orbits (from left to right) after the tracer particles are injected into the simulation. The colour range displayed is 0 to 2.5 times the mean mass surface density. All panels have the same colour display range. The  $x$  and  $y$  axes are in units of the Toomre wavelength and the entire shearing box is shown. The simulation parameters are listed in Tables 1 and 2.

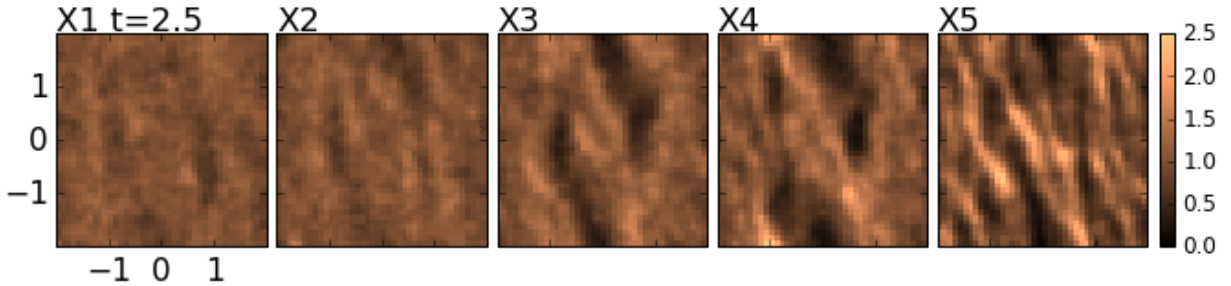


**Figure 3.** For five different simulations we show the mass surface density at  $t = 2.5$  orbits after tracer particles are injected into the simulation. The colour range displayed is 0 to 2.5 times the mean density. All panels have the same colour display range. The  $x$  and  $y$  axes are in units of the Toomre wavelength and the entire shearing box is shown. The Toomre  $Q$ -parameters for these simulations are measured at 2.5 orbital periods after tracer particles are added to the simulation. From left to right we show high Toomre  $Q$  to low Toomre  $Q$ -parameter simulations in the X series (X1–X5). The simulation parameters are listed in Tables 1 and 2.

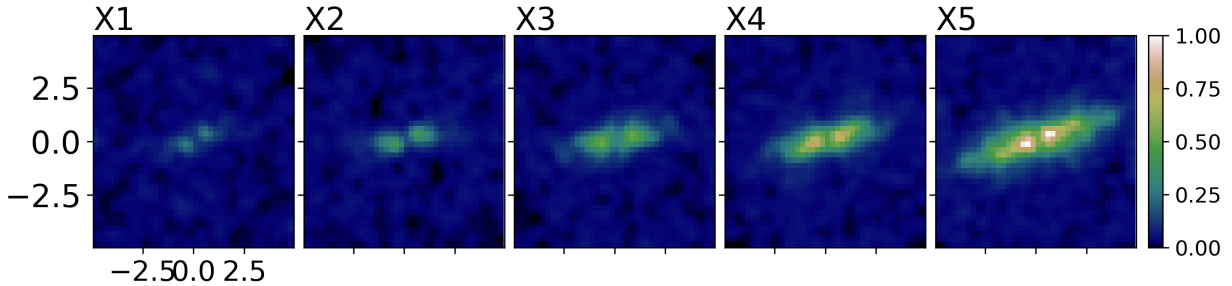


**Figure 4.** 2D Fast Fourier transforms of each of the mass surface densities shown in Figure 3 (at 2.5 orbital periods) were computed from massive particles after subtracting the mean mass surface density. The images show Fourier amplitudes and all panels have the same colour display range. The colour bar scale is set so that a sine wave with amplitude equal to the mean density gives power of amplitude 1. The centre of the image contains low frequency power. The maximum spatial frequencies (on the boundaries of each image) are  $4.91\lambda_{crit}^{-1}$  (or  $0.0049 \text{ pc}^{-1}$ ) corresponding to wavelengths of  $0.2\lambda_{crit}^{-1}$  (208 pc for  $\lambda_{crit,0} = 1007 \text{ pc}$ ). The angle of the power distribution seen in these 2D spectrograms depends on the angle of the spiral features. The lower Toomre  $Q$ -parameter simulations (on the right) have more power than the higher Toomre  $Q$ -parameter simulations. The lowest Toomre  $Q$ -parameter simulations have broad spatial frequency distributions containing power on short and long spatial wavelengths.

### 3 MIGRATION ON THE SHEARING SHEET

After listing our simulations, we discuss in section 3.1 the morphology of spiral structure. In section 3.2 we show guiding centre distributions as a function of time, illustrating spiral structure induced radial migration. As tracer parti-

cles migrate away from their birth positions, their guiding centre distributions widen. In section 3.3 the standard deviations of these distributions are shown. In section 3.4 we discuss numerical checks on the code. In sections 3.5 and 3.6 we fit functions to the standard deviations of the guid-

ing centre distributions. Maximal migration distances as a function of time are discussed in section 3.7.

We ran a series of simulations with shearing box size approximately 4 times the Toomre wavelength. Five simulations X1–X5 are run with identical parameters except with differing initial in-plane velocity dispersions for the massive particles and different levels of damping,  $\alpha$  (see Tables 1, 2). The values of damping parameter  $\alpha$  imply that damping for massive particles is slow, even for the low  $Q$  simulations. Particle positions and velocities are output every 0.5 orbital periods.

The Toomre  $Q$ -parameters are measured 2.5 orbits after the tracer particles are added to the simulation and these too are listed in Table 2. Four additional simulations were run. The X3S simulation is identical to the X3 simulation except the smoothing length is half the size of that listed in Table 1. The X3N simulation is identical to the X3 simulation except it has only 25000 massive particles instead of 50000. The X3ha and X3hb simulations are identical to the X3 simulation except X3ha has a vertical standard deviation,  $\sigma_z$ , twice that of X3 and X3hb has a vertical standard deviation half that of X3. The vertical standard deviations are computed from the  $z$  distributions of massive particles.

### 3.1 Simulation snapshots

The surface mass density of massive particles along with the positions of the 1000 massless tracer particles are shown in Figure 2 at 5 different times in the X2 simulation. The times for each snapshot are 0, 0.5, 1.0, 2.5 and 5.0 orbits after the massless tracer particles are injected into the simulation. The leftmost panel shows that spiral structure has grown prior to the insertion of our massless tracer particles. The tracer particles are inserted at  $x = 0$  where there is no drift in guiding centre position. Without spiral structure each point in the vertical green line in the leftmost panel of Figure 2 would remain fixed. The velocity shear is such that the right hand side of the box moves downward and the left hand side of the box moves upward.

One half an orbit later (second panel from left in Figure 2) the green line has become wavy as the tracer particles have been perturbed by nearby spiral structure. Perturbations excite epicyclic motions as well as move guiding centres so the width of the  $x$  distribution is only approximately equivalent to the width of the distribution of  $x$  component of the guiding centre distribution. By the end of the simulation (rightmost panel) the tracer particles have become dispersed. We do track boundary crossings for the tracer particles in case migration is extensive. However, with our shearing box length exceeding the Toomre wavelength and within 5 orbital periods, we saw no shear box boundary crossings in the  $x$  direction. Tracer particles did not cross from the right hand side to the left or vice versa. Tracer particles do cross from the top to the bottom boundary (and vice versa) due to the velocity shear.

A comparison between the leftmost three panels in Figure 2 show that the spiral structure has some coherence over an orbit. However spiral arms vary (as a function of time) in position and amplitude or strength. A difference between a shearing sheet simulation and an N-body simulation of a full disc is that in the shearing sheet there cannot be coupling of patterns from one radius to another. All spiral features are

nearly corotating with the background velocity shear (this is also discussed by Toomre & Kalnajs 1991). We have verified this by plotting density slices from the shearing box versus time. Using particles in the centre of the image (at  $x = 0$ ) we construct a density histogram giving densities as a function of  $y$  and  $t$ . There is little structure in this density histogram image as expected for patterns moving at corotation with the velocity shear in the box. Likewise, at  $x < 0$  or  $x > 0$  in a  $y$  vs  $t$  density histogram image we do see streaks due to the velocity shear. Bumps in the density field from spiral arms move approximately with the background shear velocity field, as would be expected from corotating patterns.

A comparison between the leftmost and rightmost panel in Figure 2 shows that the spiral structure is not uniform across the five orbits. The Toomre  $Q$ -parameter does change across the simulation (ranging from 1.3 to 1.6), and the spiral structure has higher density peaks and larger wavelength at later times. Our procedure for damping particles has not completely stabilized the disc. We attribute the slow evolution to the slower growth of wavelengths that differ from the peak wavelength favored by swing amplification. We keep in mind that slow variations in spiral structure in the simulations make it more difficult to predict properties of the distributions of the  $x$ -component of the guiding centre for the tracer particles as a function of time.

In Figure 3 we show the surface density distribution for X1–X5 simulations in order of decreasing Toomre  $Q$ -parameter (from left to right) but at  $t = 2.5$  periods after the tracer particles are inserted into the simulation. These snapshots illustrate that spiral structure is higher amplitude for the low Toomre  $Q$ -parameter simulations. The variation in density contrast between simulations is larger than the slow drifts during each individual simulation. Even though there are slow drifts in Toomre  $Q$ -parameter and spiral morphology across each simulation, there should be large differences in the migration rates of the tracer particles as the simulations span a large range in spiral amplitude.

We compute two-dimensional Fourier transforms of the images shown in Figure 3 and show the Fourier amplitudes in Figure 4. Our figure 4 resembles the similarly computed Figures 3 and 4 by Toomre & Kalnajs (1991) for their shearing sheet simulations. These were interpreted as showing particle-particle spatial correlations due to spiral *wakes* (Julian & Toomre 1966) and are caused by amplification of small over-densities by self-gravity (Julian & Toomre 1966; Toomre 1981). There is more power in the lower Toomre  $Q$ -parameter simulations than the high Toomre  $Q$ -parameter simulations. The lowest Toomre  $Q$ -parameter simulation (rightmost panel) has a much broader spatial frequency distribution containing power on short and long spatial wavelengths. Hence the spiral structure is not restricted to a single wavelength and a single amplitude associated with it. If we used a low order Fourier decomposition to model the spiral structure we would likely underestimate heating (in epicyclic amplitude) and migration rates.

### 3.2 Distributions of guiding centres

To characterize migration we measure the distribution of the  $x$  component of the guiding centre,  $x_g$ , for massless tracer particles as a function of time. The  $x$  component of the guid-

ing centre is computed using equations A4 from tracer particle positions and velocities. As tracer particles initially all have  $x_g = 0$ , the distributions at later times are sensitive to the extent of migration. Spiral structures could cause the guiding centre  $x_g$  of a particle to oscillate about a mean value (e.g., see Figure 4 by [Comparetta & Quillen 2012](#)).

We consider migration to be a drift in the  $x_g$  mean value, ignoring short period oscillations about this mean, however both short timescale oscillations and longer timescale drifts would affect the guiding centre distributions. We assume that the distributions are dominated by the slow drifts and so illustrate migration, though the short timescale oscillations could affect the distributions at early times. Our initial tracer particle distribution is a delta function at  $x_g = 0$ . A wider initial distribution can be considered a sum of narrow spikes each with a different initial  $x_g$ . The distribution in  $x_g$  at a later time for a wider initial distribution can be estimated by convolving the distribution we find at the same later time (derived from our initially narrow distribution) with the function describing the initial wider  $x_g$  distribution.

Guiding centre distributions are shown for the X3 simulation at 0.5, 2.5 and 5 orbital periods after tracer particle insertion in Figure 5. The distributions are normalized so they integrate to 1. Individual spikes at early times are likely caused by individual spiral features, with the distributions becoming smoother at later times. These were also noted by [Toomre & Kalnajs \(1991\)](#) who described them as guiding centre ‘bunchings.’ Below we measure the standard deviations of these guiding centre distributions but will refer to this figure later to discuss the tails of the distribution. The tails are relevant for estimating how far a particle can get from its birth guiding centre radius.

Figure 5 shows that guiding centre distributions broaden in only five rotation periods. The original spiral heating ([Carlberg & Sellwood 1985](#); [Jenkins & Binney 1990](#)) and migration models ([Sellwood & Binney 2002](#)) were mediated by growth and disappearance of individual spiral patterns. If the growth and disappearance of a spiral pattern requires a few orbital periods then within five rotation periods there is only time for one or two patterns to appear and disappear. The guiding centre distributions are smooth enough at later times that they could be consistent with a diffusive model, valid in the limit where perturbations to the  $x$ -component of the guiding centres occur randomly and many times, not just once or twice. The diffusive behavior can be reconciled with the short timescale if individual spiral features are uncorrelated or if patterns interfere with one another (as proposed by [Comparetta & Quillen 2012](#)). A re-examination of the simulations by [Toomre & Kalnajs \(1991\)](#) suggest that each swing amplified structure, seen by growth and variation in Fourier amplitude, also moves the guiding centers of groups of particles<sup>2</sup>. Stochastic variation in guiding centers may be a local process associated with swing amplification of weak density variations that are present in our simulations because of numerical noise associated with the finite particle number, but also present in the Galaxy from molecular clouds and star clusters.

<sup>2</sup> Agris Kalnajs, private communication

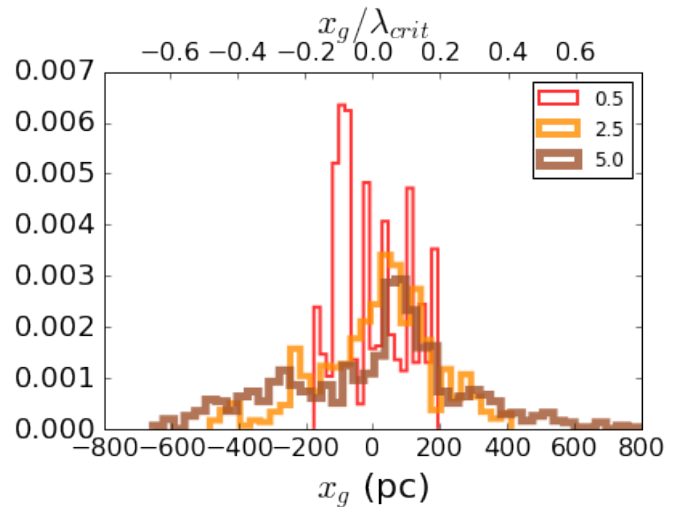


**Figure 5.** Distribution of the  $x$  component of the tracer particle guiding centres,  $x_g$ , at three times in the X3 simulation. All tracer particles had initial  $x_g = 0$ , as shown in Figure 3. The thin red line is at  $t = 0.5$  orbital periods, the mid-weight orange line at 2.5 orbital periods and the thick brown line at 5 orbital periods. The  $x$  axis is shown in units of pc for a mean surface density  $\Sigma_0 = 10M_{\odot}\text{pc}^{-2}$  (bottom axis) and in units of Toomre wavelength  $\lambda_{crit}$  (top axis). The distributions are normalized so that they integrate to 1. The width of the distributions increases in time. At later times the distributions are smooth enough that a diffusive approximation might be valid, despite the short timescale.

### 3.3 Broadening of the guiding centre distributions

We measure the standard deviation  $\sigma_{x_g}$  of the  $x$  component of the guiding centre,  $x_g$ , for the tracer particles as a function of time and these are plotted for the X1–X5 simulations in Figure 6. The standard deviations characterize the width of the distributions shown in Figure 5. Even for the strongest spiral structure (the X15simulation), within 5 orbital periods the standard deviation in  $x_g$  remains less than half a Toomre wavelength.

Figure 6 shows that the distributions of the  $x$  components of the guiding centres rapidly spread within the first orbital period. The rapid growth is likely because our tracer particles were begun in circular orbits and inserted abruptly into a simulation with spiral structure. We experimented with starting our tracer particles with velocities near those of massive particles (moving with the spiral structure) or starting them at the beginning of the simulation with the massive particles but saw similar standard deviations early in the simulation. The X3 simulation reaches a maximum of  $\sigma_{x_g}/\lambda_{crit} \approx 0.26$  and this can be compared to the maximum reached by a single tracer particle (out of 1000) of  $\sim 0.7$  as shown in Figure 5.

Figure 6 shows that the width of the guiding centre distributions depends on the Toomre  $Q$ -parameter even at early times in the simulation. The rate that the standard deviation of the distribution  $\sigma_{x_g}$  increases is large at the beginning then decreases past one orbital period. The rates that  $\sigma_{x_g}$  increases past  $t = 1$  period are shallower for the higher Toomre  $Q$ -parameter simulations. We discuss possible ex-

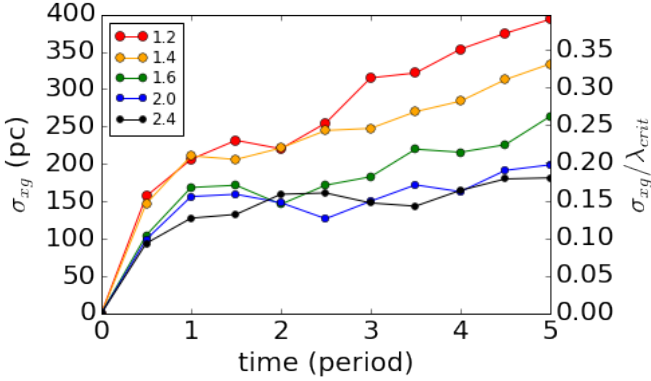


**Figure 6.** We show the standard deviation  $\sigma_{xg}$  of the  $x$  component of the tracer particle guiding radii as a function of time for X1–X5 simulations also shown in Figure 3. Higher Toomre  $Q$ -parameter simulations have less and slower radial migration. The simulations are labelled by their Toomre  $Q$ -parameter value mid-simulation (see Table 2). From top to bottom the simulations are X5 (red points), X4 (orange), X3 (green), X2 (blue) and X1 (black). The  $y$  axis is shown in units of pc for a mean surface density  $\Sigma_0 = 10M_{\odot}\text{pc}^{-2}$  (left axis) and in units of Toomre wavelength  $\lambda_{crit}$  (right axis).

planations for this. As particles increase in epicyclic amplitude, they may be less likely to be migrated by corotating spiral features (Daniel & Wyse 2015). To explore this possibility, mean epicyclic amplitudes for the same simulations as a function of time are shown in Figure 7. The epicyclic amplitudes are not large enough that multiple spiral features are crossed by single particles in their orbits. Figure 7 shows that tracer particles in the lower Toomre  $Q$ -parameter simulations have higher epicyclic amplitudes. The lower Toomre  $Q$ -parameter simulations have stronger spiral structure and so would exhibit increased heating (Carlberg & Sellwood 1985; Jenkins & Binney 1990). If the extent of migration decreases as the epicyclic amplitudes increases (as the probability for capture into resonance decreases; see section 2.3 by Daniel & Wyse 2015), the slope in  $\sigma_{xg}(t)$  for the low Toomre  $Q$ -parameter simulations would be shallower rather than higher as seen in Figure 6. The trend is opposite to that expected if the slope variation is due to a decrease in migration rate caused by an increase in epicyclic amplitude.<sup>3</sup>

A second possible explanation for the steeper slopes at lower Toomre  $Q$ -parameter past  $t = 1$  period (seen in Figure 6) is that the higher Toomre  $Q$ -parameter simulations have slower variations in spiral morphology (amplitudes and pattern speeds) than the lower Toomre  $Q$ -parameter simulations. If the spiral amplitudes increase more rapidly in the low Toomre  $Q$ -parameter simulations then the migration rate also would increase throughout the simulation. The most likely explanation for the differences in slope at later times in Figure 6 are differences in time dependent spiral structure morphology.

<sup>3</sup> In contrast re-analysis of the the shearing sheet simulations by Toomre & Kalnajs (1991) shows that the guiding center distribution standard deviations are insensitive to initial particle epicyclic amplitude; Agris Kalnajs, private communication.

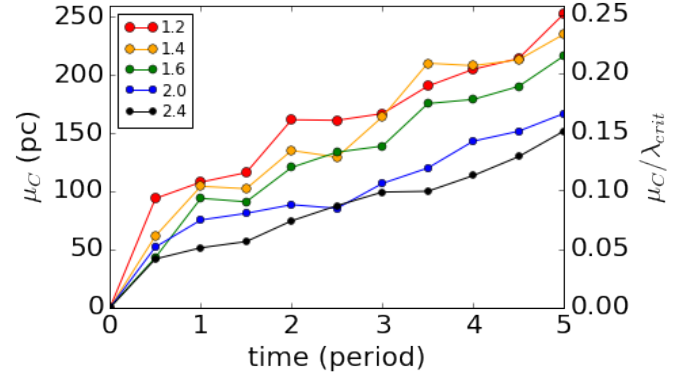


**Figure 7.** Mean epicyclic amplitude for tracer particles as a function of time for the X1–X5 simulations. The simulations are labelled by their Toomre  $Q$ -parameter value mid-simulation with points as in Figure 6. The  $y$  axis is shown in units of pc for a mean surface density  $\Sigma_0 = 10M_{\odot}\text{pc}^{-2}$  (left axis) and in units of Toomre wavelength  $\lambda_{crit}$  (right axis).

### 3.4 Sensitivity to disc thickness

Before we explore models for the time dependence of the guiding centre distributions we check the sensitivity of the simulations to vertical thickness, particle number and smoothing length. Figure 8 shows standard deviations (of  $x_g$ ) for 4 simulations that are similar to the X3 simulation (see Table 2). Compared to the X3 simulation, the X3S simulation has half the smoothing length, the X3N simulation has half the number of massive particles, and the X3ha and X3hb simulations have twice and half as thick discs. Figure 8 shows that our simulations are not strongly sensitive to the smoothing length (comparing X3S to X3) or number of particles (comparing X3N to X3). However the migration rates are sensitive to the disc thickness, with the thinner disc (X3hb) having more extensive migration. The sensitivity of the standard deviations to disc thickness will be discussed further at the end of section 3.5.

Up to this point we have discussed simulations with tracers initially placed in the midplane. We ran a simulation similar to the X3 simulation but with tracer particles begun with the same vertical dispersion ( $\sigma_z$ ) as the massive particles. The standard deviations of  $x_g$  displayed no significant differences compared to the X3 simulation.

### 3.5 Guiding centre standard deviations at 1 orbital period

Our simulation snapshots (Figures 2, 3) and Fourier amplitudes (Figure 4) show that the simulations are poorly described by a single spiral wavelength. Measurements of the peak mass surface density in the sheet as a function of time wildly fluctuated, possibly because of interference between spiral features. For a more robust measurement of spiral strength we use the standard deviation of the mass surface density distribution divided by the mean surface density  $\sigma_{\Sigma}/\mu_{\Sigma}$  and refer to this quantity as the surface density contrast. It is 0 for a uniform surface density disc and increases with the strength of spiral structures. The surface density

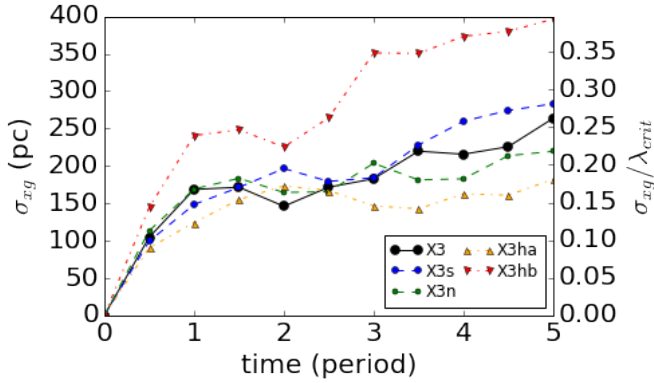


**Figure 8.** We show the standard deviation  $\sigma_{xg}$  of the  $x$  component of the tracer particle guiding radii for the simulations X3, X3S, X3N, X3ha, and X3hb. The standard deviations are not strongly sensitive to the smoothing length (comparing X3S to X3) or number of particles (comparing X3N to X3), but are sensitive to the disc thickness (comparing X3ha, X3hb to X3). The  $y$  axis is shown in units of pc for a mean surface density  $\Sigma_0 = 10M_{\odot}\text{pc}^{-2}$  (left axis) and in units of Toomre wavelength  $\lambda_{crit}$  (right axis).

contrasts are measured for each simulation at  $t = 2.5$  orbits and listed in Table 2.

We found that the surface density contrast increases with decreasing Toomre  $Q$ -parameter in the X1–X5 simulations, as expected. Plotting this against the standard deviation  $\sigma_{xg}$  revealed a trend, similar to that found by Fujii et al. (2011) for the dependence of heating rate on Toomre  $Q$ -parameter and spiral amplitude. However the trend was not matched by the thick and thin disc simulations (X3ha, X3hb) until we also included a correction for disc thickness. This approach was also explored by Fujii et al. (2011) for disc heating.

The trend is shown in Figure 9 where we plot standard deviation  $\sigma_{xg}/\lambda_{crit}$  against a unitless form for the density contrast in the midplane

$$\delta\rho \equiv \frac{\sigma_{\Sigma} \lambda_{crit}}{\mu_{\Sigma} \sigma_z}. \quad (4)$$

In Figure 9 both quantities ( $\delta\rho$  and  $\sigma_{xg}/\lambda_{crit}$ ) are computed 1 orbit after the tracer particles are inserted into the simulation. As  $\sigma_{\Sigma}/\mu_{\Sigma}$  is a measure of the surface density contrast and  $\sigma_z/\lambda_{crit}$  characterizes the thickness of the disc, their ratio characterizes spiral feature density contrast. Figure 9 shows that the width of the distribution of the  $x$ -component of the guiding centres is related to the midplane density contrast due to spiral structure. The dot dashed line in Figure 9 shows the curve

$$f(\delta\rho) = 0.12\sqrt{\delta\rho} \quad (5)$$

which captures the trend seen with the points. The coefficient 0.12 was found by trial and error and verifying by eye that the curve follows the measurements. The dependence of the distribution on  $\sqrt{\sigma_{\Sigma}/\mu_{\Sigma}}$  is similar to that expected for a migration distance dependent on the width of the corotation resonance or if particles approximately move on equipotential curves during the first orbital period (e.g., see Figure 6 by Sellwood & Binney 2002 and Daniel & Wyse 2015). The relationship seen here between migration distance and

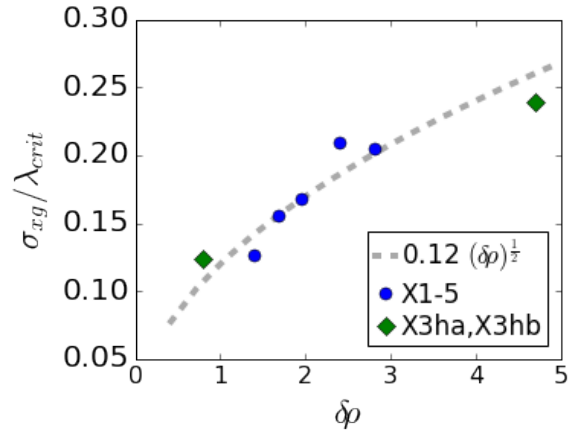


**Figure 9.** The standard deviation  $\sigma_{xg}/\lambda_{crit}$  in guiding radius for tracer particles versus midplane density contrast  $\delta\rho$  (equation 4) for simulations X1–X5, X3ha, X3hb, and X3hb, computed at a time of 1 orbit. The green diamonds show the thick and thin disc (X3ha, X3hb) simulations, whereas the blue circles are simulations X1–X5. The initial increase in guiding radius scales with density contrast. The dashed grey line shows the function in equation 5.

midplane density contrast is similar to that found previously between heating rate and spiral Fourier amplitude by Fujii et al. (2011).

The Fourier spectrograms shown in Figure 4 exhibit spatial power in a range of wavelengths. If the spiral structure only contained power at wavelengths significantly larger than the vertical scale height, the in-plane gravitational potential perturbations would be independent of scale height. However we have found that the dispersion (of  $\sigma_{xg}$  at 1 period) depends on the vertical scale height or  $\sigma_z/\lambda_{crit}$ . We attribute this dependence to the presence of spatial power in small scale spiral structure that is comparable in wavelength to the disc thickness.

In the next section, we will extend the function describing the standard deviation  $\sigma_{xg}$  at  $t = 1$  and given in equation 5 to depend on time to explore how  $\sigma_{xg}$  depends on time.

### 3.6 The time dependence of the guiding centre distribution widths

In Figure 10 we plot standard deviations of guiding radii as a function of time for simulations X1–X5, X3ha, and X3hb compared with power law curves. The curves are described by the function

$$g(\delta\rho, t) = 0.12(\delta\rho)^{\frac{1}{2}}t^{\beta} \quad (6)$$

where  $t$  is in orbital periods and we have extended equation 5 to depend on time. Three grey lines are shown in Figure 10. The topmost grey line shows the function in equation 6 evaluated using  $\delta\rho$  computed from the X5 simulation at 1 orbit and a power  $\beta = 0.4$ , and it is near the red points showing the X5 simulation. The middle grey line uses  $\delta\rho$  computed from the X3 simulation but exponent  $\beta = 0.3$  and it is near the green points showing the X3 simulation. The lower grey line has  $\delta\rho$  computed from the X1 simulation but  $\beta = 0.2$  and it is near the black points showing the X1 simulation. The X3ha, X3hb simulations are consistent with being near the bottom and top grey lines, as expected from

their density contrasts. The values of  $\beta$  for the grey lines in Figure 10 were found by plotting different values of  $\beta$  and determining by eye if they were near the measurements.

The time dependent behavior seen in the width of the guiding centre distribution  $\sigma_{xg}(t)$  suggests that the exponent  $\beta$  is higher when the spiral density contrast is higher. However further work is needed to verify this as we suspect the lower Toomre  $Q$ -parameter simulations have more rapid changes in spiral morphology during the simulation. A trend in the value of the exponent may be due to time dependent variations in the spiral density contrast as a function of time rather than how the migration rate depends on the spiral density contrast itself.

Despite its uncertainty, the exponent  $\beta$  appears to be robustly less than  $1/2$ , the expected exponent for a diffusive process giving a random walk in  $x_g$ . One possible cause for this is a reduction in migration efficiency at higher epicyclic amplitude (Daniel & Wyse 2015). Diffusive models for heating account for shallow exponents in this way (Carlberg & Sellwood 1985; Jenkins & Binney 1990). Though the dependence on epicyclic amplitude does not explain the difference in the power law exponents for the different simulations, it could account for a reduction in the values of the exponents themselves.

The migration standard deviations are higher for the X5 simulation than the X1 simulation by about a factor of 2. To estimate actual distances migrated, we multiply unitless values shown on the right hand side of Figures 10, 11 by the Toomre wavelength. As a consequence the migration distances are more sensitive to the mean surface density (through the dependence of the Toomre wavelength) than they are to the amplitude in spiral structure. As  $\lambda_{crit} \propto \Sigma/\kappa^2$  and  $\Sigma$  is likely to be exponentially dropping with increasing radius, migrations distances are likely to be further in the inner galaxy than the outer galaxy.

The dependence on a critical wavelength was previously proposed and used by Schönrich & Binney (2009) to describe ‘churning’ with a stochastic model (see their section 2.5 just above their equation 7). While we confirm a postulated strong dependence on the Toomre wavelength (often called the critical wavelength and defined in equation 1), Schönrich & Binney (2009) used a wavelength  $\lambda \equiv \sigma_{vR}Q/\kappa = \sigma_{vR}^2/(\pi G\Sigma)$  which differs from the Toomre wavelength. Perhaps there is a typographic error in their definition and they meant  $\lambda = \sigma_{vR}/(Q\kappa)$ . This when multiplied by a factor of  $2\pi$  would be equivalent to the Toomre wavelength.

### 3.7 Maximal migration rates and distances

Above we have looked at the time dependence of the width of the distributions of the  $x$  component of the guiding centres. This ignores the tails of the distribution. In section 4 below we discuss a few open clusters discovered to be both young and have super-solar metallicity. These clusters are outliers, with metallicity above most other open clusters. They could have been born interior to the Sun and migrated outward. Because they are outliers, super-solar metallicity young open clusters may have experienced more rapid migration than other clusters and so might be in the tail of the distribution of migration distances, and in a class dubbed ‘extreme migrators’ by Grand et al. (2012). In Figure 11 we

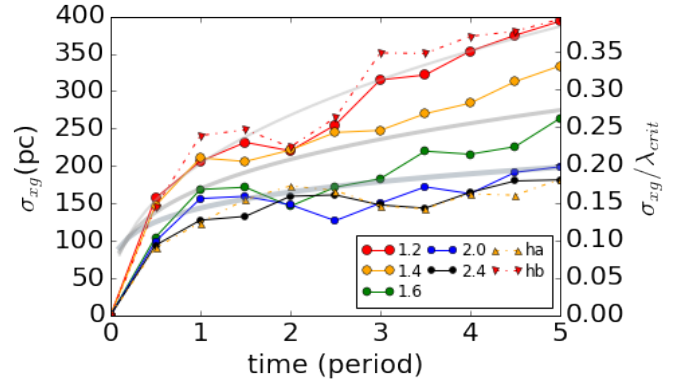


**Figure 10.** We show the standard deviation  $\sigma_{xg}/\lambda_{crit}$  of guiding radii for tracer particles as a function of time for simulations X1–X5, X3hb, and X3hb. The grey lines show functions that depend on a power of time (equation 6) with exponents 0.4, 0.3, 0.2 for each line, from top to bottom. The solid points and coloured lines for the X1–X5 simulations are identical to those previously shown in Figure 6. The  $y$  axis is shown in units of pc for a mean surface density  $\Sigma_0 = 10M_\odot\text{pc}^{-2}$  (left axis) and in units of Toomre wavelength  $\lambda_{crit}$  (right axis).

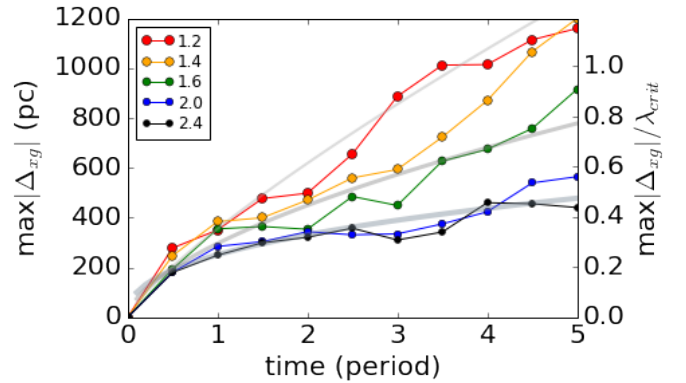


**Figure 11.** We show the maximum absolute value of the change in the  $x$  component of the guiding radius for tracer particles as a function of time for the simulations X1–X5. The grey lines show functions that depend on a power of time (equation 7) with exponent 0.8, 0.6, 0.4 for each line from the top to bottom one. The exponents used are twice those of the curves shown in Figure 10. Colours for the lines and points are the same as in Figure 6 and 10. The  $y$  axis is shown in units of pc for a mean surface density  $\Sigma_0 = 10M_\odot\text{pc}^{-2}$  (left axis) and in units of Toomre wavelength  $\lambda_{crit}$  (right axis).

show the maximum of the absolute value of the change in  $x_g$  as a function of time for tracer particles in the X1–X5 simulations.

A distribution of random walkers has standard deviation that grows with  $\sqrt{N}$  where  $N$  is the number of steps, but the maximum distance that a walker can travel is proportional to  $N$ . The maximum distance is the square of the standard deviation and this remains true as a function of time. The steeper slopes seen in the extreme values shown in Figure 11 compared to the standard deviations in Figure 6 could be due to this scaling. The grey lines on Figure 11

are curves given by a function similar to that describing the standard deviations, equation 6),

$$h(\delta\rho, t) = 0.21(\delta\rho)^{\frac{1}{2}}t^{2\beta}. \quad (7)$$

The exponents for each line in Figure 11 are twice those used in Figure 10. The comparative time dependent behavior of standard deviation and maximum are similar to that expected from diffusive-like behavior. Since the exponents for time are double for the maximum than for the standard deviation of the  $x_g$  distribution, we tried using a function  $\propto \delta\rho$  instead of  $\propto (\delta\rho)^{\frac{1}{2}}$ . However a function  $\propto \delta\rho$  did not match the numerical measurements as well as one  $\propto (\delta\rho)^{\frac{1}{2}}$ . Perhaps the process that sets the guiding centre distribution at 1 orbit differs from the subsequent diffusive behavior.

In an axisymmetric disc galaxy, a star in a circular orbit has a constant vertical component of angular momentum as it rotates around the galaxy. A spiral arm gives a non-axisymmetric (dependent on the azimuthal angle) and time dependent perturbation on the star. Instantaneously the torque on the star caused by the spiral pattern is

$$\dot{L} = \frac{\partial V_s}{\partial \theta}$$

where  $V_s$  is the perturbation to the gravitational potential caused by the pattern, and  $L$  is the vertical component of angular momentum. As  $L \sim rv_c$  for  $v_c$  the velocity of rotation and  $r$  the guiding radius, the torque corresponds to a migration rate in radius  $\dot{r} \sim \dot{L}/v_c$ . A maximal migration rate can be estimated from this torque assuming that the star stays near and on one side of the spiral arm, either leading or lagging the arm, and as shown to be true for the rapid migrators identified in simulations by Grand et al. (2012); Comparetta & Quillen (2012). Using a Gaussian bar model for a spiral arm, Comparetta & Quillen (2012) estimated that a linear density enhancement in the disc surface density with peak density  $\Sigma_p$  and oriented with a pitch angle  $\gamma$  could cause a maximal migration rate

$$\dot{r}_{max} \sim G(\Sigma_p - \mu_\Sigma)2\sqrt{\pi}\Omega^{-1} \sin \gamma \quad (8)$$

$$= \lambda_{crit}\Omega \left( \frac{\Sigma_p - \mu_\Sigma}{\mu_\Sigma} \right) \frac{\kappa^2 \sin \gamma}{\Omega^2 2\pi^{\frac{3}{2}}} \quad (9)$$

$$\approx 2 \text{ kpc Gyr}^{-1} \left( \frac{\Sigma_p - \mu_\Sigma}{10M_\odot \text{pc}^{-2}} \right) \left( \frac{\sin \gamma}{\sin 24^\circ} \right) \times \left( \frac{\Omega}{30 \text{ km s}^{-1} \text{kpc}^{-1}} \right)^{-1} \quad (10)$$

(see their section 4.3). Here the pitch angle  $\gamma$  is the angle between the ridge of peak density and the direction of rotation. This angle is the same as that used to characterize spiral arms and the angle is small for a spiral arm that is tightly wound.

We can replace  $\Sigma_p - \mu_\Sigma$  in equation 10 with the standard deviation of the surface density distribution  $\sigma_\Sigma$  measured in our simulations and write the maximum migration rate in units of critical wavelength per rotation period,  $\lambda_{crit}/P$

$$\frac{\dot{r}_{max}}{\lambda_{crit}P^{-1}} \approx \sin \gamma \frac{\sigma_\Sigma}{\mu_\Sigma}. \quad (11)$$

In our shearing sheet  $\gamma$  is the angle between a linear spiral feature's ridge of peak density and the  $y$  axis. The tilt angle of spiral structures in the shearing sheet simulations are  $\approx 30^\circ$  so for our shearing sheet simulations  $\sin \gamma \sim 1/2$ .

With surface density contrast  $\frac{\sigma_\Sigma}{\mu_\Sigma}$  ranging from 0.2 to 0.5 (listed in Table 2), the maximum migration rates we expect in our simulations are  $\sim 0.1$  to  $0.25\lambda_{crit}$  per period, giving a distance of 0.5 to  $1.25\lambda_{crit}$  in 5 periods. Even though the time dependence of the maximum distance migrated is not linear (the curves in Figure 11 range from  $\propto t^{0.4}$  to  $t^{0.8}$ ), the Gaussian bar model estimate for the *maximum* migration rate is similar to those measured in our simulations.

To achieve a maximal migration rate a particle would have to be continuously leading (or lagging) spiral features. There is a limit on the distance a particle can migrate. If we simulate an increasingly larger number of tracer particles we should not see larger and larger maxima in the migration distances. Likewise, increasing the number of stars observed would not necessarily let us find stars that have migrated larger distances (past the maximum), though stars perturbed by other mechanisms could be found (such as those ejected from the galactic centre).

#### 4 APPLICATION TO OPEN CLUSTERS

As discussed previously there are only weak constraints on the density contrast in spiral structure in the solar neighbourhood. Above we have related the maximum migration distance to two quantities, a surface density contrast arising from spiral structure and the Toomre wavelength. We discuss super-solar metallicity open clusters to attempt to place constraints on the spiral structure density contrast in the Galaxy.

The tracer particles in our simulations are point masses. When applying the results of our shearing sheet simulations to open clusters, we neglect the size of the open clusters and assume that their masses are sufficiently small that individually they have not significantly perturbed spiral arms. Cluster dissolution (e.g., Gieles et al. 2007; Martinez-Barbosa et al. 2016) is neglected.

A compilation from the literature of age, orbit and [Fe/H] for super-solar metallicity open clusters that are younger than 1 Gyr old is listed in Table 3. We use the notation in brackets to indicate abundances relative to the Sun, i.e.,  $[X/Y] = \log(X/Y) - \log(X/Y)_\odot$  and we use iron, or [Fe/H], to characterize metallicity. We list apocentre and pericentre radii ( $R_a, R_p$ ) for each cluster computed by Gozha et al. (2012). With an epicyclic approximation, the  $z$  component of the angular momentum is set by the guiding radius  $R_g$ , which is approximately the midpoint radius;  $R_g \approx (R_a + R_p)/2$ . The difference between current guiding radius and birth guiding radius would be a migration distance.

Using the metallicity gradient in [Fe/H] of  $\approx -0.07$  dex/kpc for stars younger than 4 Gyr by Anders et al. (2017) to estimate open cluster birth radii. This gradient is based on low galactic latitude red giants with astero-seismic estimated ages. See section 5 and Figure 5 by Anders et al. 2017 for a discussion on the sensitivity of the gradient to age and a comparison of their estimated gradient to those of other stellar populations, including Cepheids. Taking a mean value of [Fe/H]  $\approx 0.0$  near  $R_\odot$ , the gradient -0.07 dex/kpc and the metallicity listed in Table 3, we estimate that NGC 6583 would have been born at a galactocentric radius of 2.5 kpc. Taking its current mean galactocentric radius as its guiding

**Table 3.** Super solar open clusters younger than 1 Gyr

cluster	$R_a$ kpc	$R_p$ kpc	$e$	$z_{max}$ kpc	age Gyr	[Fe/H] dex
NGC 6583	6.6	5.4	0.09	0.13	1 <sup>a</sup>	0.4 <sup>b</sup>
Berkeley 81	5.9	4.9	0.09	0.19	0.9 <sup>c</sup>	0.23 <sup>c</sup>
NGC 2632	8.6	6.8	0.12	0.10	0.67 <sup>d</sup>	0.16 <sup>d</sup>
NGC 6067	7.6	6.8	0.06	0.07	0.090 <sup>e</sup>	0.19 <sup>e</sup>
NGC 2232	8.3	7.8	0.03	0.05	0.032 <sup>f</sup>	0.27 <sup>g</sup>

Apocentre  $R_a$ , pericentre  $R_p$  radii, orbital eccentricity  $e$  and maximum  $z_{max}$  of the Galactic orbit are those by [Gozha et al. \(2012\)](#) except for Berkeley 81. For Berkeley 81,  $e$ ,  $z_{max}$  agree with that by [Vande Putte et al. \(2010\)](#). For Berkeley 81 we show the apocentre and pericentre radius computed using the mean orbital radius of 5.4 kpc estimated by [Magrini et al. \(2015\)](#). References for ages and metallicities: <sup>a</sup>([Carraro et al. 2005](#)); <sup>b</sup>([Magrini et al. 2010](#)); <sup>c</sup>[Magrini et al. \(2015\)](#); <sup>d</sup>[Cummins et al. \(2017\)](#); <sup>e</sup>[Alonso-Santiago et al. \(2017\)](#); <sup>f</sup>[Silaj & Landstreet \(2014\)](#); <sup>g</sup>[Monroe & Pilachowski \(2010\)](#);

**Table 4.** Maximal migration rates

cluster	$R_g$ kpc	$R_{birth}$ kpc	$d_{mig}$ kpc	age orbits	migration rate kpc/Gyr
NGC 6583	6.0	2.5	3.5	6.5	3.5
Berkeley 81	5.4	4.9	0.5	6.5	0.5
NGC 2632	7.7	5.9	1.8	3.4	2.7
NGC 6067	7.2	5.4	1.7	0.5	19
NGC 2232	8.0	4.3	3.6	0.16	120

The mean or guiding radius is estimated as  $(R_a + R_p)/2$ . Birth radius,  $R_{birth}$ , is estimated using the [Fe/H] listed in Table 3,  $R_g$  and the metallicity gradient  $-0.07$  dex/kpc ([Anders et al. 2017](#)). The migration distance  $d_{mig}$  is estimated as  $R_g - R_{birth}$ . The migration rate is the migration distance divided by the cluster age. The cluster age is given in orbital periods at  $R_g$  assuming a flat rotation curve and an orbital period of 210 Myr at  $R_g = 8.2$  kpc.

or mean orbital radius (the average of apocentre and pericentre radii listed in Table 3) we estimate that the cluster could have radially migrated 3.5 kpc. Using its age this gives a roughly estimated migration rate of 3.5 kpc/Gyr. Similar estimates for the maximal migration rates are listed in Table 4 for the clusters compiled in Table 3.

If the metallicities and ages for the two youngest open clusters, NGC 6067 and NGC 2232 are robust then the needed migration rate is so high that migration alone cannot account for their super-solar metallicities. As a consequence we stop discussing these two clusters in the context of migration. A local (or patchy) enrichment model (e.g., [Malinie et al. 1993](#)) might be explored to account for them.

For the other three older open clusters a migration rate of 0.5 to 3 kpc/Gyr might be required for them to be born in a higher more metal rich galactocentric radius consistent with their metallicities and subsequently migrate outward to their current guiding radii. NGC 2632, also known as the

Praesepe cluster, is similar in metallicity, age and kinematics to the Hyades cluster. [Pompeia \(2011\)](#) speculated that the Hyades is at apocentre and a 4:1 resonance with a spiral wave increases its eccentricity and allowing it to have mean radius 1kpc within  $R_\odot$  and nearer to its expected birth radius (based on its super-solar [Fe/H] abundance). If the guiding radius used in Table 2 is overestimated for NGC 2632, we would also have over estimated the maximum migration extent and rate. Berkeley 81 has guiding radius fairly near its expected birth radius so significant radial migration is not needed to account for its metallicity. NGC 6583 has a metallicity high enough to place its estimated birth radius within the Galactic bar. Either it was born within the bar and the bar helped eject it from the inner Galaxy, or it was born near the bar end and the extent of migration required is similar to that estimated above or 2-3 kpc/Gyr. NGC 6583 has such a high metallicity it must have migrated outward. The metallicities of NGC 2632 and the Hyades suggest that they might have been born at smaller galactic radii, 1 to 2 kpc smaller than their current guiding radii.

Below we use our simulations to determine what type of spiral structure can induce the migration distances and rates estimated for the three open clusters NGC 6583, NGC 2632 and the Hyades (with similar kinematics to NGC 2632).

Our simulation figures show distance in units of the Toomre wavelength and in pc for a mean surface density of  $\Sigma_0 = 10 M_\odot \text{pc}^{-2}$  (corresponding to a Toomre wavelength of  $\lambda_{crit,0} = 1007$  pc). To estimate standard deviations in radial migration distances and maximal migration distances we must multiply distances from our Figures in units of the Toomre wavelength by the Toomre wavelength for the disc that is causing the migration. Alternatively we can use the distances in pc if we multiply them by the ratio of surface densities (the ratio of the disc that is causing the migration to  $\Sigma_0 = 10 M_\odot \text{pc}^{-2}$  or the ratio of the Toomre wavelength of the disc causing the migration to  $\lambda_{crit,0} = 1007$  pc). Curves fitting both standard deviations and maximal migration distances also depend on the square root of the spiral density contrast (as in equations 6 and 7). At a fixed surface density (mass per unit area), and using an exponential vertical density profile, the density (mass per unit volume) in the midplane is inversely proportional to the vertical scale height. Thickness of galactic components are often given in terms of a scale height  $h$  assuming the density distribution is proportional to  $\text{sech}^2(z/h)$  (expected for an isothermal, self-gravitating disk) or  $\exp(-|z|/h)$  (expected for isothermal stars or gas in a constant gravitational field). The density profile of our simulations does not have a sharp peak at  $z = 0$  and is self-gravitating so we estimate the scale height of our simulations from the standard deviation of the  $\text{sech}^2$  function, giving standard deviation  $\sigma_z \approx 0.9h$ . So the scale heights in our simulations can be estimated using values for  $\sigma_z$  in Table 1 with  $h \approx 1.1\sigma_z$ . We can correct for a difference in disc thickness, the Galactic disc as compared to that of our simulations, with a factor that depends on the square root of the ratio of scale heights (that of the disc causing the migration and that used in the simulation). Thus we can predict migration distances using our figures if we multiply them by a factor that depends on the ratio of the Toomre wavelength (compared to 1007 pc) times the square root of the ratio of scale heights.

We contrast the role of large amplitude variations in a

lower mean surface density gas disc with the role of smaller amplitude variations in a higher surface density stellar disc. We start by predicting migration distances caused by a gas disc. Our vertical standard deviation for our simulations was  $\sigma_z \approx 150$  pc (see Table 1) corresponding to a scale height of about  $h \sim 165$  pc. This exceeds a gas scale height (for molecular and cold atomic hydrogen) in the solar neighbourhood of about 100 pc (McKee et al. 2015). The surface density in molecular and cold atomic hydrogen in the solar neighbourhood is somewhat lower than  $\Sigma_0 = 10M_\odot\text{pc}^{-2}$ , or about  $\Sigma = 7M_\odot\text{pc}^{-2}$  (McKee et al. 2015). We can use distances in our figures in units of pc if we correct these distances by the ratio of  $\Sigma/\Sigma_0 = 7/10$  (for the Toomre wavelength) and by the ratio of  $\sqrt{165/100}$  to take into account the difference between the gas scale height and that of the simulations. The two corrections to the X1–X5 simulations approximately cancel each other out ( $7/10 \times \sqrt{165/100} \approx 0.9$ ), so we can use the distances in pc in our figures directly for comparison to open cluster estimated migration distances. As we expect large variations in gas density due to spiral structure we choose the simulation with highest density contrast or the X5 simulation for comparison.

After 3 orbital periods the standard deviation in  $x_g$  in the X5 simulation would be only about 300 pc and at 5 periods, 400pc (from inspection of Figure 10. The most extreme outliers have a maximum migration distance of about 900 pc at 3 periods and 1.2 kpc at 5 periods (using Figure 11). These migration distances are not larger enough to account for the estimated needed distances for migration for NGC 2632 (Praesepe) and Hyades clusters (we estimated 1.8 kpc over 700 Myr or 3.4 orbital periods). Likewise we fall short for NGC 6583 (needing 3.5 kpc at 1 Gyr but in the inner galaxy, at 6 orbital periods). We conclude that spiral structure in the gas disc *alone* cannot induce sufficient migration to account for young super-solar metallicity open clusters.

The stellar surface density is higher than the gas surface density. Taking a value for the stellar surface density of about  $\Sigma \approx 33M_\odot\text{pc}^{-2}$  (taking the value for  $\Sigma_*$  from Table 3 by McKee et al. 2015), the Toomre wavelength is  $\lambda_{crit} \approx 3.3$  kpc, exceeding by a factor of about 3 the value we used to give distances in units of pc in our figures. At this Toomre wavelength the standard deviation in the  $z$  density distribution in the X series simulations is  $\sigma_z = 500$  pc (multiplying the value from Table 1 by the Toomre wavelength) or a vertical scale height of  $h \sim 550$  pc. The stellar scale height is about 400 pc in the solar neighbourhood (taking values for M dwarfs by McKee et al. 2015). We should correct distances in our simulations by the square root of the scale height ratio or 1.17. We should correct distances in pc in our figures by the square root of the scale height ratio or 1.17 and by  $\Sigma/\Sigma_0 = 3.3$  to take into account the Toomre wavelength, or a factor of about  $1.17 \times 3.3 \sim 3.8$ .

Figure 12 and Figure 13 show maximal migration distances and standard deviations in guiding centre for the X1–X5 simulations rescaled by the factor 3.9. The spiral amplitudes in stars would be lower than for the gas, perhaps similar to the X3 simulation. We will discuss this choice in the next three paragraphs. Using the X3 simulation we take values in pc at 3 orbits and 5 orbits from Figure 12 and 13, giving standard deviations  $\sigma_{xg} = 0.8$  and 1.0 kpc, and the maximum migration distances 2.0 and 3.1 kpc. These val-

ues exceed those estimated for the gas disc. Even though the gas density might have larger density variations, we estimate that low amplitude spiral structure in the more massive stellar disc causes more radial migration.

With ages corresponding to 3 orbital periods, the Hyades and Praesepe clusters require about 1.8 kpc of migration from their birth radii, and this is similar to the maximum migration distance seen in the X3 simulation. To illustrate this we have placed a black square onto Figure 12 to represent these two clusters. The standard deviation of the guiding centre distribution estimated from our simulations (0.8 kpc at 3 orbital periods) is below that required for these two clusters, but this would be consistent with the rarity of super-solar metallicity open clusters in the solar neighbourhood (as the standard deviation must be lower than the absolute value of the maximum migration distance). At 5 orbital periods the maximum distance reached (using the X3 simulation) is 3.1 kpc and this is similar to that required to account for NGC 6583, which is shown as a black diamond on Figure 12. The standard deviation at 5 orbital periods is about 1kpc. So at 1 Gyr most clusters would lie within 1 kpc of their birth radius, putting NGC 6583 in the tail of the distribution. Were we to use a higher mean surface density, appropriate in the inner galaxy, our estimated maximum migration distance would be even larger. In summary the maximum migration distances estimated from the X3 simulation are sufficient to account for migration distances estimated for these three young and super-solar metallicity open clusters.

Above we estimated that after 1 Gyr, clusters born at the same radius would have a standard deviation in galactic radius due to migration of about 1 kpc. Using the radial metallicity gradient by Anders et al. (2017), this 1 kpc distance corresponds to a variation in metallicity of about 0.07 dex. So we would estimate that the standard deviation of metallicities of young open clusters would be the same, or about 0.07 dex in  $[\text{Fe}/\text{H}]$ . We compare this number to the standard deviation in  $[\text{Fe}/\text{H}]$  of young open clusters. From the 88 open clusters with high-quality spectroscopic data that were compiled by Netopil et al. (2016), 38 have mean galactic radius ( $R_g$ ) within 7–9 kpc, and ages less than 1Gyr (see their Figure 6 showing the radial metallicity distributions). The standard deviation in  $[\text{Fe}/\text{H}]$  for these 38 clusters is 0.074 dex (where we have used values for  $[\text{Fe}/\text{H}]$  based on the high-quality spectroscopic data from Table A1 by Netopil et al. 2016). Thus our estimate for the metallicity dispersion induced by migration, using the X3 simulation, is consistent with that observed. Had we used a lower or higher Toomre  $Q$ -parameter simulations for comparison (X1, X2 or X4, X5) the predicted standard deviation in radial migration distances would not have agreed with the young open cluster standard deviation in  $[\text{Fe}/\text{H}]$ . The density contrast present in the X3 simulation is consistent both with the dispersion in  $[\text{Fe}/\text{H}]$  and the few super-solar metallicity young open clusters that represent rarer more extreme migrators.

Figure 13 shows that after 1 orbital period, the standard deviation in guiding centre coordinate  $x_g$  does not increase rapidly with time. Consequently taking into account the open cluster age distribution (for clusters older than 1 Gyr) would not significantly increase the estimated metallicity dispersion arising from migration. We have not numerically studied migration at times longer than 5 orbital

periods, but the slow increase in the standard deviation as a function of time seen in our simulations would be consistent with the absence of a strong correlation between open cluster age and metallicity (the age-metallicity relation; e.g., Carraro et al. 1994; Yong et al. 2012; Netopil et al. 2016). In other words, the scatter in  $[\text{Fe}/\text{H}]$  due to migration could exceed the slow increase in metallicity due to ongoing large scale enrichment in the disc. Our estimates for the metallicity scatter neglects local (patchy) enrichment of the ISM (Balsler et al. 2015; Berg et al. 2015; Vogt et al. 2017; Krumholz & Ting 2018) and this additional process might be required to account for very young open clusters such as NGC 6067 and NGC 2232 (and the high  $[\alpha/\text{Fe}]$  cluster NGC 6705; Magrini et al. 2014, 2015; Casamiquela et al. 2017b) that could not have migrated far enough to account for their abundances.

In summary, the rare super-solar metallicity open clusters near the Sun appear to be consistent with a stellar density contrast (for spiral arms) similar to that of the X3 simulation or with a surface density contrast  $\sigma_\Sigma/\mu_\Sigma \sim 0.26^{+0.08}_{-0.04}$ . Here we have taken the value for  $\sigma_\Sigma/\mu_\Sigma$  for the X3 simulation (listed in Table 2). For the uncertainty we have taken the difference between the density contrast in the X4 and X3 simulations (+0.08) and between the X2 and X3 simulations (-0.04). The inferred extent of recent radial migration at this density contrast is also consistent with the standard deviation in  $[\text{Fe}/\text{H}]$  for young open clusters. Were we to use a lower value for the metallicity gradient of 0.06 dex/kpc, estimated migration distances for the clusters would increase by about 20% and our estimated density in stellar density contrast in spiral arms would be larger but within the higher end of the +0.08 uncertainty.

Our spiral arm surface density contrast level  $\sigma_\Sigma/\mu_\Sigma \sim 0.26^{+0.08}_{-0.04}$  somewhat exceeds that estimated from the Galactic COBE model (Drimmel & Spergel 2001) with peak above mean divided by mean  $(\Sigma_p - \mu_\Sigma)/\mu_\Sigma \approx 0.16 \pm 0.03$ . Here we have taken the number based on the K-band spiral amplitude discussed at the end of section 6 by Drimmel & Spergel (2001) and used the  $\pm 18\%$  uncertainty listed in their Table 2. As discussed by Drimmel & Spergel (2001), the COBE model measurement is dependent on the type of model used to fit the COBE data and lower than that expected based on imaging studies of other galaxies, so perhaps we should not be concerned that our density for the local density contrast is higher than that previously measured. Also, as we will discuss in section 5, there are a number of reasons our estimate is not precise.

In section 3.7 we gave in equation 10 an estimate for the maximal migration rate using the Gaussian bar model (Comparetta & Quillen 2012). We now compute the maximum migration migration rate in the Solar neighborhood estimated with this model. With an angular rotation rate in the Solar neighborhood  $\Omega_\odot \approx 30 \text{ km s}^{-1} \text{ kpc}^{-1}$  (Bland-Hawthorn & Gerhard 2016), spiral density contrast  $(\Sigma_p - \mu_\Sigma)/\mu_\Sigma \approx 0.16$  based on the COBE data model (Drimmel & Spergel 2001), and a mean stellar surface density  $\mu_\Sigma \approx 33 M_\odot \text{ pc}^{-2}$  (McKee et al. 2015), the maximum migration rate is  $\dot{r}_{max} \sim 0.5 \text{ kpc Gyr}^{-1}$  for a pitch angle of  $12^\circ$  and about  $1 \text{ kpc Gyr}^{-1}$  for a pitch angle of  $24^\circ$ , spanning the pitch angle estimates compiled by Vallee (2008). These maximal migration rates are lower than the required open cluster migration rates listed in Table 4 for NGC 6583,

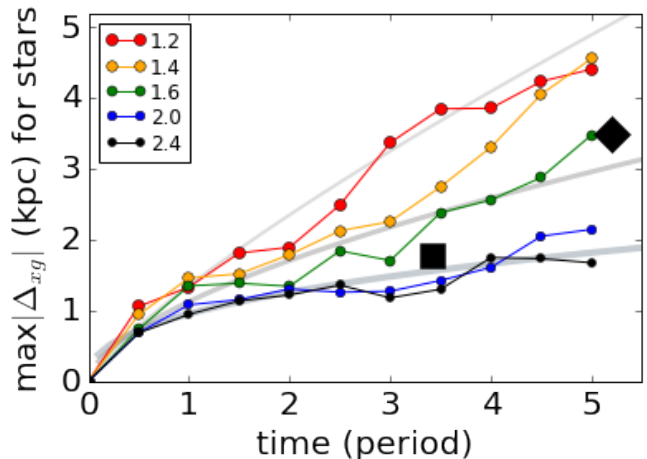


**Figure 12.** We show the maximum absolute value of the change in the  $x$  component of the guiding radius for tracer particles as a function of time for the simulations X1–X5, but now scaled to a stellar disc of  $\Sigma = 30 M_\odot \text{ pc}^{-2}$  and with vertical scale height similar to the Galactic thin disc. The black square shows estimated migration distances for NCC 2632 (Praesepe) and Hyades clusters. The black diamond shows estimated migration distance for NGC 6583. The black square is placed at the age of the NCC 2632 and Hyades clusters in orbits. The black diamond should be at 6.5 orbits but this lies off our integrations so we have placed it at 5.2 orbits. The grey lines and circles are from the X1–X5 simulations and the same as in Figure 11. This figure shows that a simulation with spiral density contrast similar to the X3 simulation has maximal migration distances similar to the super-solar metallicity Praesepe, Hyades and NGC 6583 open clusters.

and the Praesepe and Hyades open clusters. This rough estimate for the maximal migration rate supports our inference that the spiral density contrast in the solar neighborhood could be higher than that estimated by the COBE model.

## 5 DISCUSSION AND SUMMARY

We use shearing sheet N-body simulations to investigate how far stars and open clusters can migrate in a galaxy disc within 5 orbital periods. The simulations contain massive particles that exhibit spiral structure due to their own self-gravity. Massless tracer particles are inserted into the simulation after spiral structure has grown. Due to perturbations from the spiral structures, guiding centres of the tracer particles drift. This drift corresponds to radial migration in a disc galaxy. As a function of time, we measure the width and maximum of the distribution of the changes in guiding centres for tracer particles.

The shearing sheet simulations suggest that the rate and extent of radial migration is primarily set by the Toomre or critical wavelength. As this wavelength is set by the mean surface mass density, migration rates and extent should be higher in the inner regions of galaxies than the outer regions. We find that in 5 rotation periods, the standard deviations of the guiding centre distributions broaden to between 0.2 and 0.4 of the Toomre wavelength with a maximum migration distance (in guiding centre  $x$  component) about three times this.

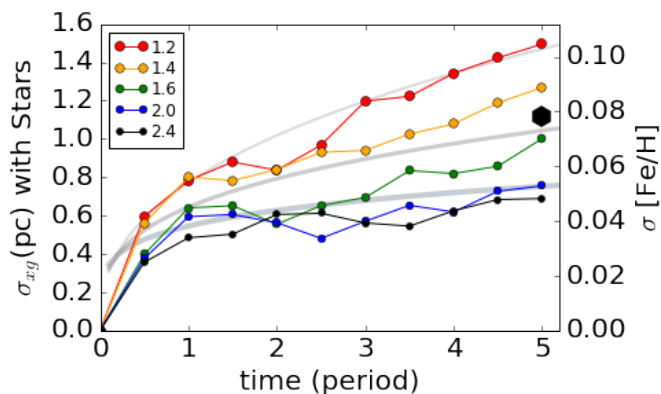


**Figure 13.** We show the standard deviation  $\sigma_{xg}$  of guiding radii for tracer particles as a function of time for simulations X1–X5, but now scaled to a stellar disc of  $\Sigma = 30M_{\odot}\text{pc}^{-2}$  and with vertical scale height similar to the Galactic thin disc. The grey lines and circles are from the X1–X5 simulations and the same as in Figure 11. The right axis has converted units of distance to variation in  $[\text{Fe}/\text{H}]$  using the metallicity gradient by [Anders et al. 2017](#) of  $-0.07$  dex/kpc. The black hexagon shows the standard deviation in metallicities for 38 open clusters with high-quality spectroscopic data that were compiled by [Netopil et al. \(2016\)](#). This figure shows that a simulation with spiral density contrast similar to the X3 simulation predicts a standard deviation in migration distance consistent with the metallicity scatter in young open clusters.

To a lesser extent migration rates depend on the surface density or midplane density contrast in the spiral structure. The standard deviations of the guiding centre distributions can be described by power laws with exponents in the range 0.2 to 0.4. The maximal distances obey exponents twice those of the standard deviation suggesting that a diffusive model may describe the behavior of the guiding centre distributions. A diffusive model could operate on such a short time if individual spiral features are uncorrelated or if patterns interfere with one another. We attribute the variation in the exponents in different simulations to slow variations in the spiral morphology that was more rapid in our lower Toomre  $Q$ -parameter simulations.

We used our simulations and estimated guiding radii for super-solar metallicity open clusters to attempt to constrain the surface density contrast in spiral structure at the Sun’s galactocentric radius. The comparison suggests that the surface density contrast has ratio of standard deviation to mean  $\sigma_{\Sigma}/\mu_{\Sigma} \sim 1/4$  with an uncertainty of about 30%, and with value somewhat exceeding the COBE model by [Drimmel & Spergel \(2001\)](#).

Our estimate for the density contrast is uncertain for a number of reasons. Spiral structure in our simulations remains near corotation. In contrast, galactic simulations of a disc often show patterns that move with different frequencies (e.g., [Quillen et al. 2011](#)). Spiral spiral patterns can influence each other or be coupled to a galactic bar. A bar or spiral pattern that is distant from its corotation might still affect radial migration ([Brunetti et al. 2011](#); [Minchev et al. 2012](#)). Nearby features could interfere causing peaks to drift in radius or increase and decrease in amplitude (e.g., as described by [Quillen et al. 2011](#)). It is difficult to say

whether these effects would increase or decrease the extent of radial migration compared to that predicted using the shearing sheet. Perhaps a study similar to [Fujii et al. \(2011\)](#) that focused on heating could improve upon estimates for migration using complete disc simulations.

The expression for the Toomre wavelength (equation 1) implies that near the Sun’s galactic radius,  $R_{\odot}$ , the Toomre wavelength is large,  $\lambda_{crit} \sim R_{\odot}$ . The shearing sheet approximates a local patch of a rotating disc (in polar coordinates) with a Cartesian square (see Figure 1) and neglects radial gradients in epicyclic frequency, mass surface density and velocity dispersion. While shearing sheet simulations are internally consistent (in that their spiral structure is evolving due to their own self-gravity) they may not be a good approximation for applications, such as discussed here, requiring a shear box size similar to or larger than the associated galactic radius or the disc scale length. Full disc simulations are required to improve upon applications derived from shearing sheet simulations. The Toomre wavelength, though it is a locally computed quantity, may also be relevant to larger scale spiral morphology. [D’Onghia \(2015\)](#) proposed that the Toomre wavelength locally sets the number of spiral arms, hence the large Toomre wavelength computed at and within the Sun’s galactic radius could account for the small number of spiral arms (2 to 4) within the Sun’s galactic radius.

Our simulations only contain point masses. A gas and stellar disc could behave differently than the phenomena we see in pure N-body simulations. Our tracer particles were inserted abruptly into a simulation containing spiral structure with an ad hoc damping to help reduce Toomre  $Q$ -parameter variations in the disc. Their initial velocity is not a good match to those of recently born stars. The Galaxy is comprised of multiple populations, each with a different scale height. We have neglected this structure, relating the migration rate only to a vertical dispersion and a spiral density contrast. Future numerical studies could reduce these errors and uncertainties with more detailed simulations. While open clusters facilitate measurement of both metallicities and ages, their distributions may be biased if cluster number and evaporation and destruction are correlated with age, birth radius or metallicity. Uncertainties in cluster orbit, metallicity, the extent of local ISM enrichment or abundance variations, and the metallicity gradient also affects estimated migration distances. Better numerical simulations would allow more detailed observations and improved measurements of young stars and open clusters to be placed quantitatively in context with improved models for migration.

ACQ is grateful to the Leibniz-Institut für Astrophysik

Potsdam for their warm welcome and hospitality July 2017, Mt. Stromlo observatory for their warm welcome and hospitality Nov 2017– Jan 2018, and support from the Simons Foundation. This material is based upon work supported in part by the National Science Foundation Grant No. PHY-1460352, for the University of Rochester’s Department of Physics and Astronomy REU program. C.C. acknowledges support from DFG Grant CH1188/2-1 and from the ChETEC COST Action (CA16117), supported by COST (European Cooperation in Science and Technology). We thank Marica Valentini, Friedrich Anders, Charlie Lineweaver, Agris Kalnajs, Mark Krumholz, and David Hogg for helpful discussions. We are grateful to Agris Kalnajs for making his conference proceeding available to us electronically and for re-examining his shearing sheet simulations from 1991.

## REFERENCES

- Alonso-Santiago, J., Negueruela, I., Marco, A., Taberner, H. M., Gonzalez-Fernandez, C., & Castro, N. 2017, MNRAS, 469, 1330
- Anders, F., et al. 2017, A&A, 600, A70
- Asplund, M., Grevesse, N., Sauval, A. J., & Scott, P. 2009, ARA&A, 47, 481
- Anthony-Twarog, B. J., Deliyannis, C. P., Twarog, B. A., Cummings, J. D., & Maderak, R. M. 2010, AJ, 139, 2034
- Athanassoula, E. 1984, PhR, 114, 319
- Balsler, D. S., Wenger, T. V., Anderson, L. D., & Bania, T. M. 2015, ApJ, 806, 199
- Barnes, J., & Hut, P. 1986, Nature, 324, 446
- Benjamin, R. B., et al. 2005, ApJ, 630, L149
- Berg, D. A., Skillman, E. D., Croxall, K. V., Pogge, R. W., Moustakas, J., & Johnson-Groh, M. 2015, ApJ, 806, 16
- Bland-Hawthorn, J. & Gerhard, O. 2016, ARA&A, 54, 529
- Bland-Hawthorn, J., Krumholz, M. R., & Freeman, K. 2010, ApJ, 713, 166
- Binney, J. & Tremaine, S. 1987, *Galactic Dynamics*, Princeton University Press, Princeton NJ.
- Brunetti, M., Chiappini, C. & Pfenniger, D. 2011, A&A, 534, 75
- Carlberg, R. G., & Sellwood, J. A. 1985, ApJ, 292, 79
- Cantat-Gaudin, T., et al. 2014, A&A 569, A17
- Cantat-Gaudin, T., Donati, P., Vallenari, A., Sordo, R., Bragaglia, A., & Magrini, L. 2016, A&A, 588, A120
- Carretta, E., Bragaglia, A., & Gratton, R. G. 2007, A&A, 473, 129
- Carraro, G., & Chiosi, C. 1994, A&A, 287, 761
- Carraro, G., Mendez, R. A., & Costa, E. 2005, MNRAS, 356, 647
- Casamiquela, L., et al. 2017, MNRAS, 470, 4363
- Casamiquela, L., et al. 2017, accepted for publication in A&A, arXiv171011069
- Casagrande, L., Schönrich, R., Asplund, M. et al. 2011, A&A 530, A138
- Chiappini, C., Matteucci, F. & Romano, D., 2001, ApJ 554, 1044
- Chiappini, C., Romano, D., & Matteucci, F. 2003, MNRAS, 339, 63
- Chiappini, C. 2009, in The Galaxy Disk in Cosmological Context, IAU Symposium 254, eds. Andersen, J., Nordström, B. and Bland-Hawthorn, J., p. 191–196
- Comparetta, J. & Quillen, A. C. 2012, astro-ph/1207.5753
- Cummings, J. D., Deliyannis, C. P., Maderak, R. M., & Steinhauer, A. 2017, AJ, 153, 128
- Daniel, K. J. & Wyse, R. F. G 2015, MNRAS 447, 3576
- De Silva, G. M., Sneden, C., Paulson, D. B., Asplund, M., Bland-Hawthorn, J., Bessell, M. S., & Freeman, K. C. 2006, AJ, 131, 455
- D’Onghia, E., 2015, ApJL, 808, L8
- Drimmel, R. & Spergel, D. N. 2001, ApJ, 556, 181
- Flynn, C., Holmberg, J., Portinari, L., Fuchs, B., & Jahreiss, H. 2006, MNRAS, 372, 1149
- Feng, Y., & Krumholz, M. R. 2014, Nature, 513, 523
- Friel, E. D. 1995, ARA&A, 33, 381
- Friel, E. D., Jacobson, H. R., & Pilachowski, C. A., 2010, AJ, 139, 1942 Abundances of Red Giants in Old Open Clusters. V. Be 31, Be 32, Be 39, M 67, NGC 188, and NGC 1193
- Fuchs, B. 2001, A&A, 368, 107
- Fujii, M. S., Baba, J., Saitoh, T. R., Makino, J., Kokubo, E., & Wada, K. 2011, ApJ, 730, 109
- Gieles, M., Athanassoula, E., & Portegies Zwart, S. F. 2007, MNRAS, 376, 809
- Gozha, M.L., Borkova, T.V., & Marsakov, V.A. 2012, Astron. Lett., 38, 506
- Grand, R. J. J., Kawata, D., & Cropper, M. 2012, MNRAS, 421, 1529
- Haywood, M., Di Matteo, P., Lehnert, M. D., Katz, D., & Gomez, A. 2013, A&A, 560, A109
- Jacobson, H. R. et al. 2016, A&A 591, A37
- Janes, K. A. 1979, ApJS, 39, 135
- Jenkins, A., & Binney, J. 1990, MNRAS, 245, 305
- Jilkova, L., Carraro, G., Jungwiert, B., & Minchev, I. 2012, A&A, 541, A64
- Julian, W. H., & Toomre, A. 1966, AJ, 146, 810
- Krumholz, M. R., & Ting, Y.-S. 2017, MNRAS, in press, arxiv1708.06853
- Loebman, S. R., Debattista, V. P., Nidever, D. L., et al. 2016, ApJ, 818, L6
- Loebman, S. R., Roskar, R., Debattista, V. P., et al. 2011, ApJ, 737, 8
- Ma, J. 2002, A&A, 388, 389
- Maderak, R. M., Deliyannis, C. P., Anthony-Twarog, B. J., Twarog, B. A., Cummings, J. D., King, J. R., & Steiman-Cameron, T. Y. 2015, AJ, 149, 141
- Magrini, L., Randich, S., Zoccali, M., et al. 2010, A&A, 523, 11
- Magrini, L. et al. 2014, A&A, 563, A44
- Magrini, L. et al. 2015, A&A, 580, A85
- Magrini, L. et al. 2017, A&A, 603, A2
- Malinie, G., Hartmann, D. H., Clayton, D. D., & Mathews, G. J. 1993, ApJ, 413, 633
- Martinez-Barbosa, C.A., Brown, A.G.A., Boekholt, T., Portegies Zwart, S., Antiche, E., & Antoja, T. 2016, MNRAS, 457, 1062
- Martinez-Medina, L.A., Pichardo, B., Peimbert, A., & Carigi, L. 2017, MNRAS, 468, 3615
- McKee, C. F., Parravano, A., & Hollenbach, D. J. 2015, ApJ, 814, 13
- Minchev, I., Chiappini, C., & Martig, M. 2013, A&A, 558, A9
- Minchev, I., Chiappini, C., & Martig, M. 2014, A&A, 572, A92
- Minchev, I., Famaey, B., Quillen, A. C., Di Matteo, P., Combes, F., Vljajic, M., Erwin, P., & Bland-Hawthorn, J. 2012, A&A, 548, A126
- Minchev, I., Famaey, B., Combes, F., Di Matteo, P., Mouhcine, M., & Wozniak, H. 2011, A&A, 527, A147
- Minchev, I., & Famaey, B. 2010, ApJ, 722, 112
- Monroe, T.R., & Pilachowski, C.A. 2010, AJ, 140, 2109
- Netopil, M., Paunzen, E., Heiter, U., & Soubiran, C. 2016, A&A, 585, A150
- Nieva, M.-F., & Przybilla, N. 2012, A&A, 539, A143
- Pancino, E., Carrera, R., Rossetti, E., & Gallart, C. 2010, A&A, 511, A56
- Peterson, R. C., & Green, E. M. 1998, ApJ, 502, 39
- Pompeia, L. et al. 2011, MNRAS, 415, 1138
- Przybilla, N., Nieva, M.-F. & Butler, K. 2008 ApJ, 688, L103

- Quillen, A. C., Dougherty, J., Bagley, M. B., Minchev, I., & Com-  
paretta, J. 2011, MNRAS, 417, 762
- Rein, H., & Tremaine, S. 2012, MNRAS, 415, 3168
- Rein, H., & Liu, S.-F. 2012, A&A, 537, A128
- Roskar, R., Debattista, V. P., Quinn, T. R., Stinson, G. S., &  
Wadsley, J. 2008, ApJ, 684, L79
- Roskar, R., Debattista, V. P., Quinn, T. R., & Wadsley, J. 2012,  
MNRAS, 426, 2089
- Safronov, V. S., 1960, Annales d'Astrophysique, 23, 979
- Sellwood, J. A., & Binney, J. J. 2002, MNRAS, 336, 785
- Schönrich, R., & Binney, J. 2009, MNRAS, 396, 203
- Silaj, J., & Landstreet, J.D. 2014, A&A, 556, A132
- Soubiran, C. 1999, Ap&SS, 265, 353
- Stanghellini, L., & Haywood, M. 2010, ApJ, 714, 1096
- Toomre, A. 1981, in Structure and Evolution of Normal Galaxies,  
ed. S. M. Fall & D. Lynden-Bell (Cambridge: Cambridge Univ.  
Press), 111
- Toomre, A. 1964, ApJ, 139, 1217
- Toomre, A. & Kalnajs, A. J. 1991, in "Dynamics of Disc Galaxies",  
Edited by Björn Sundelius, Göteborg, Sweden, p. 341-358.
- Vallée, J. P. 2008, AJ, 135,1301
- Vande Putte, D., Garnier, T. P., Ferreras, I., Mignani, R. P., &  
Cropper, M. 2010, MNRAS, 407, 2109
- Vera-Ciro, C., D'Onglia, E., Navarro, J. F. 2016, ApJ, 833, 42
- Wielen, R. 1977, A&A, 60, 263
- Wielen, R., Fuchs, B., & Dettbarn, C. 1996, A&A, 314, 438
- Vogt, F. P. A., Perez, E., Dopita, M. A., Verdes-Montenegro, L.,  
& Borthakur, S. 2017, A&A, 601, A61
- Yong, D., Carney, B. W., & Friel, E. D. 2012, AJ, 144, 95

## APPENDIX A: THE SHEARING SHEET APPROXIMATION

The Hamiltonian for the shearing sheet is

$$H(p_x, p_y; x, y) = \frac{p_x^2}{2} + \frac{p_y^2}{2} - 2p_y\Omega x + \frac{\kappa^2 x^2}{2}. \quad (\text{A1})$$

The momenta  $p_x, p_y$  are canonical and conjugate to the co-ordinates  $x, y$ . The epicyclic frequency  $\kappa$  determines the frequency of oscillations in the  $x$  direction. This Hamiltonian can be derived by writing a 2D Hamiltonian for particle motion in cylindrical coordinates for motion in the plane and transforming to a frame rotating with the disc at a particular radius. A patch is chosen centered at this radius. The Hamiltonian is then expanded to second order in coordinates from the center of the disc patch and to second order in canonical momenta. In celestial mechanics this is known as Hill's approximation (e.g., Rein & Tremaine 2012) and is equivalent to a classic epicyclic approximation (e.g., Binney & Tremaine 1987).

This Hamiltonian gives equations of motion

$$\begin{aligned} x &= x_g + C \cos(\kappa t + \phi_0) \\ v_x &= -C\kappa \sin(\kappa t + \phi_0) \\ y &= c - \frac{(4\Omega^2 - \kappa^2)}{2\Omega} x_g t - \frac{2\Omega}{\kappa} C \sin(\kappa t + \phi_0) \\ v_y &= -\frac{(4\Omega^2 - \kappa^2)}{2\Omega} x_g - 2\Omega C \cos(\kappa t + \phi_0). \end{aligned} \quad (\text{A2})$$

Here particle velocities  $v_x = \dot{x}, v_y = \dot{y}$ . The orbit can be described in terms of a guiding centre,  $x_g, y_g$  and epicyclic oscillations  $x_s, y_s$  about the guiding centre  $x = x_g + x_s; y = y_g + y_s$ . The parameter  $C$  can be recognized as a constant epicyclic amplitude and the parameter  $\phi_0$  as a phase (see

for example section 3.2.3 by Binney & Tremaine 1987). The guiding centre  $x_g$  position is also a constant. The  $y_g$  guiding centre coordinate drifts depending on the velocity shear,

$$y_g = c - \frac{(4\Omega^2 - \kappa^2)}{2\Omega} x_g t \quad (\text{A3})$$

where the parameter  $c$  is a constant. With zero epicyclic amplitude  $y = c - \frac{(4\Omega^2 - \kappa^2)}{2\Omega} x t$ , the velocity is solely in the  $y$  direction  $\dot{y} = -\frac{(4\Omega^2 - \kappa^2)}{2\Omega} x$  and depends only on  $x$  (see Figure 1).

It is often useful to compute the guiding centre position in terms of current positions and velocities

$$\begin{aligned} y_g &= y - y_s = y - \frac{2\Omega}{\kappa^2} v_x \\ &= y - \frac{\Omega^2}{\kappa^2} 2\Omega^{-1} v_x \\ x_g &= x - x_s = \frac{4\Omega^2}{\kappa^2} x + \frac{2\Omega}{\kappa^2} v_y \\ &= \frac{\Omega^2}{\kappa^2} (4x + 2\Omega^{-1} v_y). \end{aligned} \quad (\text{A4})$$

The epicyclic amplitude  $C$  and phase  $\phi$  can then be computed using the guiding  $x_g$  and positions and velocities with

$$\begin{aligned} C^2 &= (x - x_g)^2 + v_x^2/\kappa^2 \\ \phi &= \kappa t + \phi_0 = \text{atan2}(-v_x/\kappa, x - x_g) \end{aligned} \quad (\text{A5})$$

where the inverse tangent function is used to compute angles in all quadrants.

### A1 Modification to the SEI integrator

We modify the equations in section 3.5 by Rein & Tremaine 2012 for the SEI integrator so that a non-Keplerian value of the epicyclic frequency  $\kappa$  can be used. Rein & Tremaine (2012) denote  $x^n, y^n, v_x^n, v_y^n$  for the positions and velocities at timestep  $n$ . Their equations 9 for the centre of epicyclic motion are modified as follows with factors of  $\Omega/\kappa$ :

$$\begin{aligned} x_0^n &= \frac{\Omega^2}{\kappa^2} (2v_y^n + 4x^n) \\ y_0^n &= y^n - \frac{\Omega^2}{\kappa^2} 2v_x^n \Omega^{-1}. \end{aligned} \quad (\text{A6})$$

where  $x_0^n, y_0^n$  are the guiding centres at timestep  $n$ . The epicyclic vector (their equations 10) is modified to

$$\begin{aligned} x_s^n &= \Omega(x^n - x_0^n) \\ y_s^n &= \frac{1}{2} \frac{\kappa}{\Omega} (y^n - y_0^n). \end{aligned} \quad (\text{A7})$$

The epicyclic motion is written as a rotation and their equation 11 is modified to be

$$\begin{aligned} x_s^{n+1} &= x_s^n \cos(\kappa\Delta t) + y_s^n \sin(\kappa\Delta t) \\ y_s^{n+1} &= -x_s^n \sin(\kappa\Delta t) + y_s^n \cos(\kappa\Delta t). \end{aligned} \quad (\text{A8})$$

The guiding centre coordinates are restored by modifying their equations 12 to be

$$\begin{aligned}
 x^{n+1} &= x_s^{n+1} \Omega^{-1} + x_0^n \\
 y^{n+1} &= 2y_s^{n+1} \frac{\Omega}{\kappa} + y_0^n - \frac{1}{2} \left( 4 - \frac{\kappa^2}{\Omega^2} \right) x_0^n \Omega \Delta t \\
 v_x^{n+1} &= y_s^{n+1} \frac{\kappa}{\Omega} \\
 v_y^{n+1} &= -2x_s^{n+1} - \frac{1}{2} \left( 4 - \frac{\kappa^2}{\Omega^2} \right) x_0^n \Omega.
 \end{aligned} \tag{A9}$$

With  $\kappa/\Omega = 1$  for a Keplerian disc equations A6 - A9 are the same as the original ones by Rein & Tremaine (2012).

The `rebound` code is modified by adding a new unitless parameter `KAPPA_OMEGA`  $\equiv \kappa/\Omega$ . It is defined like `OMEGA` in `rebound.h` in the definition for the structure `struct reb_simulation_integrator_sei`. In the routine `rebound.c` we initialize `KAPPA_OMEGA = 1` so there is no change for the user wanting a Keplerian disc. In routine `boundary.c` for the cases for the shear boundary (`REB_BOUNDARY_SHEAR`) occurrences of  $\frac{3}{2}\Omega$  are modified to become  $\frac{1}{2} \left( 4 - \frac{\kappa^2}{\Omega^2} \right)$ . The SEI integrator itself in `integrator_sei.c` is modified using equations A6 - A9.

## A2 Vertical motion

The Hamiltonian in equation A1 can be extended to allow motion in the vertical direction with an additional momentum  $p_z$  and coordinate  $z$  and with an additional term added to the Hamiltonian

$$H_3(p_z, z) = \frac{p_z^2}{2} + \frac{\Omega_z^2 z^2}{2} \tag{A10}$$

where the velocity  $v_z = \dot{z} = p_z$  and  $\Omega_z$  is the vertical epicyclic frequency. The `rebound` code allows the vertical epicyclic frequency to be adjusted separately from  $\Omega$  and  $\kappa$  (see equation 13 by Rein & Tremaine 2012 and associated discussion). The equations of motion

$$\begin{aligned}
 z &= D \cos(\Omega_z t + \varphi_0) \\
 v_z &= -D \Omega_z \sin(\Omega_z t + \varphi_0)
 \end{aligned} \tag{A11}$$

where  $\Omega_z$  is the vertical epicyclic frequency, the constant  $D$  is the vertical epicyclic amplitude and  $\varphi_0$  is a phase. The vertical epicyclic frequency  $\Omega_z$  is labelled `OMEGAZ` in `rebound`. The  $z$  and  $v_z$  coordinates are updated similar to the epicyclic vector in equation A8 as shown in equation 13 by Rein & Tremaine 2012. The vertical epicyclic amplitude  $D$  and epicyclic phase  $\varphi$  can be computed from coordinate  $z$  and vertical velocity  $v_z$

$$\begin{aligned}
 D^2 &= z^2 + v_z^2 / \Omega_z^2 \\
 \varphi &= \Omega_z t + \varphi_0 = \text{atan2}(-v_z / \Omega_z, z)
 \end{aligned} \tag{A12}$$

similar to equation A5.